

RESEARCH ARTICLE

10.1002/2013WR014943

Key Points:

- Hydraulically fractured Bowland Shale unlikely poses risks to aquifers
- Horizontal mass fluxes significantly reduce pollution risks to aquifers
- Flow and solute transport approaches must be used for the risk assessment

Supporting Information:

- Readme
- Figure 1S
- Figure 2S
- Figure 3S
- Figure 4S
- Figure 5S
- Figure 6S
- Figure 7S
- Figure 8S
- Figure 9S
- Figure 10S

Correspondence to:

Z. Cai,
z.cai@qub.ac.uk

Citation:

Cai, Z., and U. Ofterdinger (2014), Numerical assessment of potential impacts of hydraulically fractured Bowland Shale on overlying aquifers, *Water Resour. Res.*, 50, 6236–6259, doi:10.1002/2013WR014943.

Received 25 OCT 2013

Accepted 3 JUL 2014

Accepted article online 9 JUL 2014

Published online 31 JUL 2014

Numerical assessment of potential impacts of hydraulically fractured Bowland Shale on overlying aquifers

Zuansi Cai¹ and Ulrich Ofterdinger¹

¹Groundwater Research Group, School of Planning Architecture and Civil Engineering, Queen's University Belfast, Belfast, Northern Ireland, UK

Abstract Natural gas extracted from hydraulically fractured shale formations potentially has a big impact on the global energy landscape. However, there are concerns of potential environmental impacts of hydraulic fracturing of the shale formations, particularly those related to water quality. To evaluate the potential impact of hydraulically fractured shale on overlying aquifers, we conduct realizations of numerical modeling simulations to assess fluid flow and chloride transport from a synthetic Bowland Shale over a period of 11,000 years. The synthetic fractured shale was represented by a three-dimensional discrete fracture model that was developed by using the data from a Bowland Shale gas exploration in Lancashire, UK. Chloride mass exchange between fractures and the rock matrix was fully accounted for in the model. The assessment was carried out to investigate fluid and chloride mass fluxes before, during, and after hydraulic fracturing of the Bowland Shale. Impacts of the upward fracture height and aperture, as well as hydraulic conductivity of the multilayered bedrock system, are also included in this assessment. This modeling revealed that the hydraulically fractured Bowland Shale is unlikely to pose a risk to its overlying groundwater quality when the induced fracture aperture is $\leq 200 \mu\text{m}$. With the fracture aperture $\geq 1000 \mu\text{m}$, the upward chloride flux becomes very sensitive to the upward fracture height growth and hydraulic conductivity of the multilayered bedrock system. In the extremely unlikely event of the upward fracture growth directly connecting the shale formation to the overlying Sherwood Sandstone aquifer with the fracture aperture $\geq 1000 \mu\text{m}$, the upward chloride mass flux could potentially pose risks to the overlying aquifer in 100 years. The model study also revealed that the upward mass flux is significantly intercepted by the horizontal mass flux within a high permeable layer between the Bowland Shale and its overlying aquifers, reducing further upward flux toward the overlying aquifers.

1. Introduction

The success of unconventional gas extracted from shale formations (shale gas) over the last decade has changed the energy landscape in the United States. Shale gas rose from 2% of U.S. gas production in 2000 to 30% in 2011, and is projected to be more than 50% by 2030. On the global scale, shale gas could increase total natural gas resources by approximately 32%, with an estimate of the total 7299 trillion cubic feet (~ 200 trillion cubic meter) technically recoverable gas worldwide [U.S. Energy Information Administration, 2013b]. This vast shale gas resource offers the opportunity for a number of regions around the world (e.g., Europe and China) to reduce their reliance on energy imports or strive toward energy independence [U.S. Energy Information Administration, 2013a]. In the United Kingdom, onshore shale gas reserve potential was first estimated to be 150 billion cubic meter by the British Geological Survey in 2010. The best shale gas potential is mainly associated with the Bowland Shale of the Pennine Basin in northern England and the Kimmeridge Clay of the Weald Basin in southern England [Harvey and Gray, 2010]. A recent study [Andrews, 2013] using 3-D modeling revised the previous estimates, with best estimate (50% probability) of total in-place gas resource of 37.6 trillion cubic meters in the Bowland Shale across central Britain (Figure 1). Although the UK government has granted several licence areas for shale gas exploration and development, only some small-scale exploratory activities (three test wells) have been reported in the Bowland Shale of the Lancashire licence areas (Figure 1). It is expected that more test wells (4–12) will be conducted for the exploration stage in the area [Broderick et al., 2011].

Shale gas mainly consists of methane, although other gases may also be present, trapped in very low permeability of sedimentary rocks. Unlike conventional gas, shale gas does not steadily flow into a well due to

Prospective UK Bowland Shale gas field

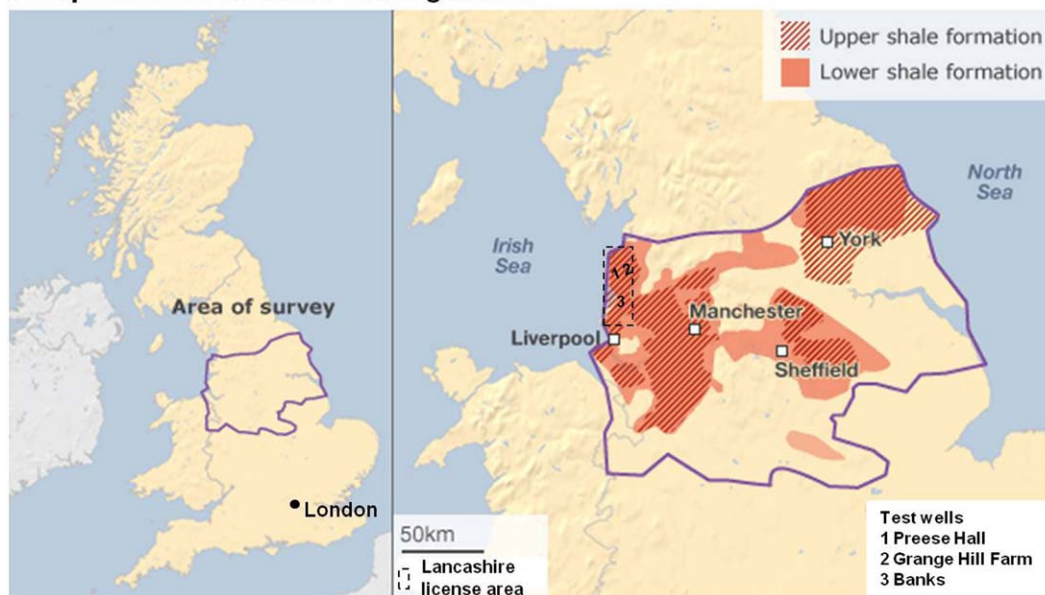


Figure 1. Location of the Bowland Shale gas target areas in central Britain and Lancashire license area [after Andrews, 2013; Broderick et al., 2011].

the low permeability of the shale units. To achieve economic gas flow rates into a production well, additional stimulation by hydraulic fracturing is required to increase the permeability of shale formations. Hydraulic fracturing involves perforation and fluid injection processes. The perforation process is to initiate fractures or holes along the horizontal well by firing explosive charges. Fluid injection aims to induce fracture growths by the high pressure injection of fracturing fluid, with a volume of around 9000–29,000 m³ per horizontal well [Broderick et al., 2011; *The Royal Society and The Royal Academy of Engineering*, 2012].

Hydraulic fracturing of the shale formations have raised concerns of environmental risks to water quality, particularly due to gas migration and contaminant transport through induced and natural fractures [Vidic et al., 2013]. A study of 60 groundwater wells in aquifers overlying the Marcellus and Utica shale formations in northeastern Pennsylvania showed that methane concentrations in drinking water in active gas extraction areas were systematically higher than those in neighboring nonextraction sites [Osborn et al., 2011]. Another study of 46 groundwater wells in southwestern Pennsylvania found that bromide and chloride concentrations, as well as hardness and other indicators, increased in one well after drilling and hydraulic fracturing [Boyer et al., 2011]. Other studies reported that hydraulic fracturing might contaminate local groundwater in West Virginia and Wyoming [DiGiulio et al., 2011; U.S. Environmental Protection Agency, 1987]. However, it is difficult to determine whether hydraulic fracturing of the shale formations has affected groundwater quality, because it requires baseline conditions and detailed information of well drilling and casing. Most importantly, complex flow and solute transport through induced and natural fractures, which are generally from over 1000 m below overlying aquifers, requires a long-term and extensive monitoring programme which is often unavailable.

With the increasing development of shale gas resources worldwide, the impact of hydraulic fracturing on groundwater quality could be increasing. Risk assessment of this impact is, however, difficult to be achieved based on a small-scale and short-term monitoring programme. To protect groundwater resources and avoid potential long-term deterioration of groundwater quality, the risk of hydraulic fracturing must be properly assessed. This risk assessment can be conducted by numerical modeling analyses of flow and transport in the fractured rock system. A recent study applied a groundwater flow model to estimate the risk of groundwater contamination from a hydraulically fractured shale by using particle tracking method [Myers, 2012]. The study concluded that hydraulic fracturing could create high upward advective flow in the fracture and advective travel time between the shale formations to overlying aquifers could be less than 10 years. However, there were concerns of Myers' [2012] modeling framework of neglecting critical hydrologic processes

and misrepresenting physical flow boundary conditions, which could severely compromise its conclusions [Cohen *et al.*, 2013; Sainers and Barth, 2012]. First, groundwater flow during fluid injection in Myers' [2012] work would be severely affected by the closeness of the lateral and horizontal no-flow boundaries, leading to substantial increase of the upward flow rate. Second, a single 1500 m overburden of sandstone oversimplified the hydrostratigraphy of the Marcellus Shale [Lee *et al.*, 2011; Williams, 2010], failing to represent complex flow and solute transport in the multilayered system. Finally and most importantly, upward flows in fractures were represented by a 6 m wide high-permeability column connecting the Marcellus Shale directly to the surface by using particle tracking method. The assumed 1500 m vertical fracture just represented one of the extremely rare cases of upward fracture growths. This model setting may be incapable of representing flow in an open fracture with a typical aperture of less than millimeters. In addition, the particle tracking method could not represent complex solute transport phenomena as it could not account for mass exchange between open fractures and the rock matrix.

The goal of this modeling study is to assess the potential impact of hydraulically fractured Bowland Shale on its overlying groundwater quality, using the numerical modeling of flow and solute transport in a fracture system. The approach is to conduct a parametric study to explore the importance of some key factors such as the upward fracture height growth, induced fracture aperture, and hydraulic conductivities of host rocks on upward chloride mass fluxes to overlying aquifers. Unlike Myers' [2012] work, flow and solute transport in fractured rocks were represented by a discrete fracture model. With a model domain of 5 km \times 3 km \times 3 km containing 10 different geological layers, this modeling study is to investigate the subsurface flow and transport of contaminants in relevant and realistic scenarios. We have constructed a synthetic site, which is based on data from a Bowland Shale gas exploratory test well (Preese Hall) in the Lancashire licence area (Figure 1). Published statistical data of induced fracture height growths worldwide were combined with the existing data regarding geological faults at the site to generate some possible upward fracture growth scenarios. With these fracture growth scenarios in a range of fracture aperture from 20 to 1000 μ m, risk assessment of the hydraulically fractured shale to overlying aquifers was conducted for three sets of rock permeability over 3 orders of magnitude where each hydrostratigraphic unit has unique hydraulic conductivities.

2. Methods and Scenarios

2.1. HydroGeoSphere

HydroGeoSphere is a fully integrated surface and subsurface flow and transport code [Therrien *et al.*, 2004]. The subsurface module, which is used for this study, is based on a three-dimensional (3-D) subsurface flow and transport code FRAC3DVS [Therrien and Sudicky, 1996]. FRAC3DVS is an efficient and robust numerical model that solves the three-dimensional variably saturated subsurface flow and solute transport equations in nonfractured or fractured media. For fractured media, FRAC3DVS can represent them either in equivalent porous media or in discretely fractured media manners. The equivalent porous media approach normally represents subsurface flow and solute transport in fractured media by dual-porosity or single-porosity media with equivalent permeability. For the discretely fractured media approach, the 3-D system is composed of a porous matrix, discretized with 3-D elements, and a fracture network represented by three sets of fractures. Each individual fracture is discretized with two-dimensional (2-D) elements. FRAC3DVS uses a standard time-marching Galerkin finite element approach to solve the flow and transport equations. The use of a preconditioned iterative solver and adaptive time stepping allows for the fast solution for matrix equations with tens to hundreds of thousands of unknowns. Fracture networks can be created in HydroGeoSphere by either built-in fracture generator, or deterministically by inputting an individual fracture geometry. Transport processes including advection, dispersion, sorption, and degradation in both fractures and the porous matrix are fully accounted for, as well as solute exchange between fractures and the porous matrix.

2.2. Development of a Representative Bowland Shale Scenario

In order to investigate and interpret the subsurface fate and transport of contaminants in hydraulically fractured shale, we created a numerical model which is representative of the Bowland Shale and its overlying and underlying geology. Reported data from a 2800 m vertical test well (Preese Hall, Figure 1) in Lancashire, UK [de Pater and Baisch, 2011], which has been recently completed for the shale gas exploration in the

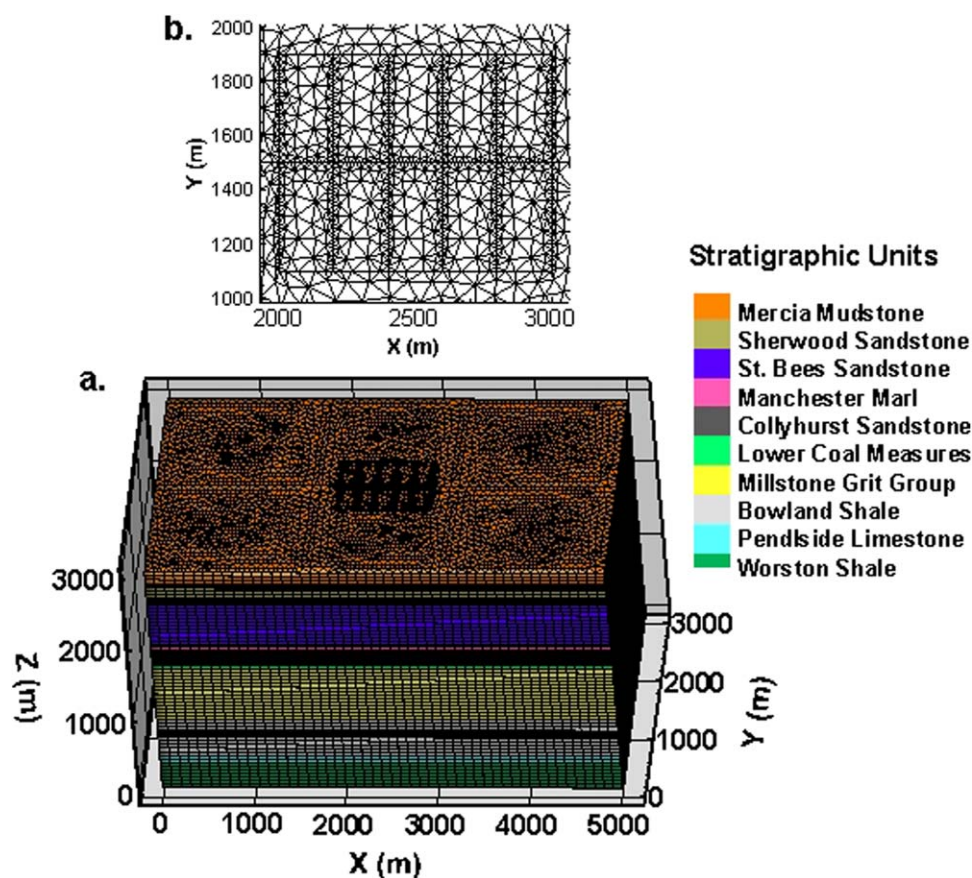


Figure 2. The stratigraphic units of the $5 \times 3 \times 3$ km 3-D model domain and model discretization (a). (b) a closeup of the finer discretization in the centre of the model domain.

region, was used as a base to build the multilayered hydrogeological model and select appropriate values of parameters such as hydraulic conductivity, porosity, and other hydraulic properties according to each identified hydrostratigraphic unit.

2.2.1. The Numerical Model of the Bowland Shale

A $5 \times 3 \times 3$ km 3-D model with 10 geological layers was created for this study (Figure 2). Depths, at which the geological layers are located, were extracted from the reported Bowland Shale gas test well in Lancashire [de Pater and Baisch, 2011] with some slight modifications to facilitate the model construction (Table 1). These 10 geological layers were assumed to extend parallel across the model domain at their respective depths. Natural upward and horizontal flows were considered for the multilayered system. The bedrock surrounding the Bowland Shale is stratified as observed in the test well data, and consists of 10 layers of interbedded shale, limestone, millstone, mudstone, coal measures, marlstone, and sandstone units. These are sedimentary rocks and the permeability of geological units is generally controlled by horizontal and vertical fractures. Due to the lack of fracture data to construct a 3-D fracture network like the study presented by Cai *et al.* [2007], initial hydraulic properties of each stratigraphic unit were represented by the equivalent porous media approach with unique porosity and permeability. The equivalent permeability of the layered system was considered to be anisotropic.

2.2.2. Selection of Values for Parameters

The selection of appropriate parameter values to represent hydraulic properties of these 10 geological layers in the model domain is a key to this study. The model consists of several layers of Permian Marlstone and Carboniferous sedimentary rocks. The hydrogeological understanding of these rocks is, unlike the chalk and Triassic sandstone in the United Kingdom, relatively poor as they attracted little attention due to the poor groundwater productivity. Furthermore, these rocks were buried 1000 m below ground surface level.

Table 1. Geological Layers of the Domain and Selected Hydraulic Parameter Values

Unit	Depth ^a (m)	Elevation ^b (m)	Typical K_h ^c ($m\ s^{-1}$)	Modeled K_h Values ($m\ s^{-1}$)	K_h/K_v ^d (-)	Porosity θ (-)	Tortuosity ^p τ (-)	Storage Coefficient S_c (-)
Mercia Mudstone Group	0–207	2800–3000	$1.0 \times 10^{-7e,f}$	$1.0 \times 10^{-8}, 1.0 \times 10^{-7}, 1.0 \times 10^{-6}$	$100^{e,g}$	$0.10^{e,g}$	0.046	1×10^{-3h}
Sherwood Sandstone Group	207–423	2600–2800	1.20×10^{-5h}	$1.2 \times 10^{-6}, 1.2 \times 10^{-5}, 1.2 \times 10^{-4}$	10^i	0.23^h	0.141	2×10^{-3h}
St. Bees Sandstone	423–1030	2000–2600	8.1×10^{-7h}	$8.1 \times 10^{-8}, 8.1 \times 10^{-7}, 8.1 \times 10^{-6}$	10^i	0.15^h	0.080	8.6×10^{-5h}
Manchester Marl	1030–1109	1900–2000	1.0×10^{-8j}	$1.0 \times 10^{-9}, 1.0 \times 10^{-8}, 1.0 \times 10^{-7}$	10^i	0.15^j	0.080	2×10^{-5j}
Collyhurst Sandstone	1109–1246	1750–1900	7.9×10^{-5h}	$7.9 \times 10^{-6}, 7.9 \times 10^{-5}, 7.9 \times 10^{-4}$	10^i	0.26^h	0.166	5×10^{-4h}
Lower Coal Measures	1246–1277	1700–1750	1.7×10^{-9j}	$1.7 \times 10^{-10}, 1.7 \times 10^{-9}, 1.7 \times 10^{-8}$	10^i	0.10^j	0.046	3.4×10^{-5j}
Millstone Grit Group	1277–2023	1000–1700	7.9×10^j	$7.9 \times 10^{-9}, 7.9 \times 10^{-8}, 7.9 \times 10^{-7}$	10^i	0.08^j	0.034	1×10^{-4j}
Bowland Shale	2023–2507	500–1000	6.0×10^{-8}	$6.0 \times 10^{-9}, 6.0 \times 10^{-8}, 6.0 \times 10^{-7i}$	10^i	0.03^k	0.009	1×10^{-4i}
Pendleside Limestone	2507–2575	400–500	$1.6 \times 10^{-6j,m}$	$1.6 \times 10^{-7}, 1.6 \times 10^{-6}, 1.6 \times 10^{-5}$	10^i	0.01^j	0.002	3×10^{-4g}
Worston Shale	2575–2744	0–400	6.0×10^{-7n}	$6.0 \times 10^{-9}, 6.0 \times 10^{-8}, 6.0 \times 10^{-7}$	10^i	0.03^k	0.009	1×10^{-4i}
Clitheroe Lst Complex	Below 2744	NR ^o	NA	NA	NA	NA	NA	NA

^aDepth below ground surface level, this data from an exploration drilling at Lancashire were original in feet and converted in meter here [de Pater and Baisch, 2011].

^bThe geological unit represented in the numerical model in the vertical (z) direction.

^c K_h means bulk horizontal hydraulic conductivity.

^d K_h/K_v is the anisotropy ratio of horizontal and vertical hydraulic conductivity.

^eHobbs et al. [2002].

^fTellam and Lloyd [1981].

^gCripps and Taylor [1981].

^hAllen et al. [1997].

ⁱGiven that these are sedimentary rocks, bedding plane fractures are believed to provide the major pathways for flow and solute transport in these rocks.

^jJones et al. [2000].

^kThe hydrogeological properties of the Bowland Shale are not available but reported values [Myers, 2012; Schulze-Makuch et al., 1999] of Marcellus Shale in the United States are adopted here for the high K case.

^lAssumed to be the same as the Millstone Grit Group.

^mHolliday [1986].

ⁿNot available and assumed to be the same as the Bowland Shale format.

^oNR means that the geological unit was not represented in the numerical model.

^pEstimated from $\tau = \theta^{4/3}$ [Millington, 1959], NA means not applicable.

The physical properties of these rocks may be different to those characterized by outcrop samples and shallow well investigations, as little weathering effects and geological stress may form different types of fracture networks in deep geological formations.

In order to account for uncertainty in estimating hydraulic parameters of these sedimentary rocks, three sets of values over 3 orders of magnitude were selected to represent bulk hydraulic conductivity of each geological layer. For other hydraulic parameters such as porosity and storage coefficient, a single typical/mean value was selected for each layer. This is because the spans of these two parameter values are much less than hydraulic conductivity and their impacts on groundwater flow and solute transport can be expected to be far less significant than hydraulic conductivity. The selected values of hydraulic parameters for the synthetic Bowland Shale domain are listed in Table 1. The main sources of the parameter values are from two key reports by the British Geological Survey [Allen et al., 1997; Jones et al., 2000], and the parameter values selected for this study are those from the field-scale observations and most relevant to the Bowland Shale site. The values of hydraulic parameters for the Bowland and Worston Shale formations are the least rigorous, as few, if any, field-scale observations of hydraulic conductivity, porosity, and storage coefficient are available. Therefore, the hydraulic properties of the Marcellus Shale [Myers, 2012; Schulze-Makuch et al., 1999] were used to represent these two shale formations. However, the reported hydraulic conductivity of the Marcellus Shale was assigned to the high hydraulic conductivity cases, as this value was ~4 orders of magnitude higher than those measured from the core samples [Soeder, 1988]. The storage coefficients of the Bowland and Worston Shales were assumed to be the same as that in the Millstone Grit Group.

A horizontal hydraulic head gradient of 5‰ was applied to the model domain, which is within the range of reported values from field observations of regional gradients at three other bedrock sites in England [Dames and Moore, 1999; Schurch and Buckley, 2002; Schurch et al., 2004]. No reports with regard to upward gradients within the Bowland Shale were available. However, data in the Lancashire test well showed that the borehole pressure at ~3000 m below ground surface was ~42,000 kPa (equivalent ~4200 m fresh water pressure). This is ~40% over the hydrostatic pressure. Overpressure was also reported in the U.S. shale formations of Utica, Marcellus, and Barnett, with a pressure gradient of 10–17 kPa/m [Gassiat et al., 2013]. This reported pressure gradient matches well with the theoretical estimate of the maximum upward head

Table 2. Key Parameters Selected for Flow and Solute Transport

Parameters	Values
Horizontal hydraulic head gradient, ΔI_x (-)	5‰
Vertical hydraulic head gradient for the lower boundary, ΔI_z (-)	250%
Longitudinal dispersivity in the rocks, $\alpha_{x,r}$ (m)	10
Transverse dispersivity in the rocks, $\alpha_{y,r}$ (m)	1
Vertical dispersivity in the rocks, $\alpha_{z,r}$ (m)	1
Fracture width, $2d$ (m)	400
Dispersivity in fracture, α_f (m)	0.5
Chloride diffusion coefficient, D^* ($m^2 s^{-1}$)	2.6×10^{-9}

gradient of 1 m brine/m (brine density: 1230 kg/m^3 at total dissolved solid of 350 g/L, temperature: 100°C). With accounting for the density gradient of brine and fresh water, the “effective” brine upward gradient of ~ 0.23 was estimated by *Flewelling and Sharma* [2014]. To implement the estimated “effective” brine upward gradient of 0.23 in the Bowland Shale, a vertical head gradient of 250% was applied for the bottom of the model domain to create an

upward flux boundary condition. A no-flow upper boundary condition was assigned for the model domain. This means that groundwater recharge is not considered in this model assessment. The reasons for the no-flow upper boundary condition are: (1) the top layer of model domain contains a 200 m thick Mercia Mudstone layer; (2) the vertical hydraulic conductivity of the Mercia Mudstone is very low (10^{-10} m/s , Table 1); and (3) very limited recharge via Mercia Mudstone were revealed by pumping tests [Jones et al., 2000]. This also suggests that the horizontal gradient is assumed to be created from the recharge area upgradient of the model area. The dispersion was assumed to be the same in all rock layers, with a selected dispersivity value of 10 m in the horizontal direction (x) and 1 m in transverse (y) and vertical (z) directions [Gelhar et al., 1992]. The parameter values selected for flow and transport in the model domain are summarized in Table 2.

2.3. Discretization and Hydraulic Boundaries

To implement the synthetic site in HydroGeoSphere, the model domain of $5 \text{ km} \times 3 \text{ km} \times 3 \text{ km}$ was discretized into 679,343 3-D elements (triangular prisms) (Figure 2). In the x-y plane ($5 \text{ km} \times 3 \text{ km}$), the domain was discretized into 6349 2-D triangular elements. In the vertical (z) direction, the 10 geological layers were discretized into 107 layers, with the variable layer thickness from 1 to 50 m. The finer discretization around the injection well areas, which locate at the center of the x-y plane (x: 2000–3000 m, y: 1000–2000 m) and the middle of the Bowland Shale formation (z: 700–800 m). This was done to ensure that the model could accurately capture the injection processes and fluid flow and solute transport in fractures propagated by the injection, as well as the mass exchange between fractures and the rock matrix. In addition to the grid refinement above, vertical refinement was also applied at the interfaces of the geological layers with distinguishing hydraulic properties. For example, vertical refinement up to 1 m a layer was used to represent the upper (z = 1750 m) and lower (z = 1700) boundaries of the Collyhurst Sandstone. This fine discretization was to limit/eliminate the numerical dispersion which could be introduced by the big contrast in hydraulic conductivity between the Collyhurst Sandstone and its adjacent layers (4 orders of magnitude between the Collyhurst Sandstone and the Low Coal Measure, and 3 orders of magnitude between the Collyhurst Sandstone and the Manchester Marl). In the horizontal direction, constant head boundaries were specified in the model domain, with constant head inflow (x = 0 m) and outflow (x = 5000 m) boundaries. The upward flow was represented by an upward flux boundary at the bottom of the domain (z = 0), by using upward head gradient and selected hydraulic conductivity for the bottom layer. The horizontal and vertical head gradients are provided in Table 2 and the remaining boundaries are impermeable.

2.4. Chloride Source Term and Reference Scenario

A constant source of chloride, which extended within the Bowland Shale and below (z: 0–1000 m), was specified in the domain. Initially, chloride concentrations were set to 0 for the rest of the domain. In the reference simulations, a steady state flow was first established, and then chloride was allowed to transport in the domain for a period of 11,000 years. The year 1000 concentration distributions were used as starting concentrations for all simulations of hydraulic fracturing scenarios. The results of the reference simulations from year 1000 to year 11,000 served as a “control” to assess impacts of hydraulic fracturing on subsurface water flow and mass fluxes in the model domain.

2.5. Simulation of Fluid Injection

A 1 km horizontal well was assumed to be used for gas extraction from the Bowland Shale in this study, and hydraulic fracturing was performed within the horizontal well. The length of the horizontal well is within the range reported in the Barnett Shale [The Royal Society and The Royal Academy of Engineering, 2012;

Zoback *et al.*, 2010]. The horizontal well was assigned at the center of the model x-y plane and within the middle of the Bowland Shale (x: 2000–3000 m; y: 1500 m, z: 750 m). In order to eliminate/minimize the boundary effects on groundwater flow during the fluid injection, the model domain was setup to ensure sufficient distances (at least 750 m) between no-flow boundaries and the horizontal well.

The fluid injection simulated 2500 m³ of fracturing fluid injection over 2 h, through six isolated segments of the horizontal well with a total length of 240 m. This is equivalent to an injection rate of 1.5 L/m of the well length per second. This injection rate is the average rate of the six-stage hydraulic fracturing in Lancashire in 2011 [de Pater and Baisch, 2011]. Each injection well segment was assumed to be located along the horizontal well with an interval of ~160 m. The length of each injection well segment was equivalent to 40 m which is in the range (18–72 m) of the field operation in Lancashire. Overall injection rate for each well segment was ~60 L/s. Each injection well segment was represented by a horizontal injection well with a well diameter of 6 in. (15.25 cm) in the model. Unlike the field operation of multistage injection, the model simulated a simultaneous injection of the 2500 m³ fluid via the six horizontal injection wells for 2 h. This can be considered as one of the worst case scenarios to assess impact of the fluid injection on the flow field. In the injection simulation, the Darcy's law was assumed to be valid during the fluid injection. Given that HydroGeoSphere cannot accommodate the deformation of rocks caused by the high fluid pressure, no fracture propagation was assumed during the injection. Instead, fracture propagation was assumed to take place immediately after the cease of fluid injection. The hydraulic head distribution at the end of the injection (hour 2), with the chloride concentration distribution at year 1000 of the reference simulation, were then used as starting heads and concentrations for all simulations of hydraulic fracturing scenarios.

2.6. Hydraulic Fracturing Scenarios Examined

Fractures propagated by hydraulic fracturing of shale formations have been monitored by several methods (e.g., tiltmeters and microseismic monitoring) over the last decade [The Royal Society and The Royal Academy of Engineering, 2012]. Data from these techniques can be fed into computer modeling to monitor real-time 3-D fracture propagation. A study of fracture treatment performed in the four U.S. major shale formations between 2001 and 2011 suggested that the hydraulic fracturing process tended to propagate many short fractures which were perpendicular to the horizontal well due to the geological stresses from the overlying rock formations [Fisher and Warpinski, 2012]. Statistical data from five United States major shale formations showed that more than 80% of vertical upward and downward fracture growths induced by hydraulic fracturing were less than 200 m. The probability of an upward propagating hydraulic fracture which extended vertically >350 m was 1% and the maximum upward fracture was ~600 m in the Barnett shale [Davies *et al.*, 2012; Fisher and Warpinski, 2012]. The longest upward hydraulic fracture was reported to be ~1000 m from offshore Nigeria [Loseth *et al.*, 2011].

In order to assess the impact of hydraulically fractured Bowland Shale on the overlying aquifers, a range of hydraulic fracturing scenarios were simulated by HydroGeoSphere to investigate the subsurface flow and mass fluxes from the source zone (the Bowland Shale and below) for a period of 10,000 years. All scenarios assumed that fracture propagation occurred immediately after the end of injection. Each segment of the injection well was assumed to create only one vertical fracture (six fractures in total) with an extensive upward growth, which would provide new pathways for upward mass fluxes toward the overlying aquifers. Hydraulic fracturing is likely to induce vertical fracture growths with uneven distributed fracture aperture. Arthur *et al.* [2008] showed in a computer simulation that hydraulic fracturing resulted in a variable fracture aperture along depths, with the largest aperture region near the horizontal well and aperture decreasing with increasing distances to the horizontal well. Given that the induced fracture aperture is likely to vary with the pressure applied during hydraulic fracturing and no reported induced aperture is available, a uniform fracture aperture was assumed in this study. A range of the fracture apertures from 20 to 1000 μm was also applied in this study to investigate the impact of fracture aperture on upward water and mass fluxes. The width of each rectangular fracture plane was assumed to be 400 m, which extended 200 m away from the injection well in the transverse direction [Zoback *et al.*, 2010]. Furthermore, the drawback of the injection fluid was not considered in this numerical assessment, which represented one of the worst case scenarios. These 6 x-z fracture planes were assigned at x = 2000, 2200, 2400, 2600, 2800, and 3000 m along the horizontal well. The vertical locations of the fracture planes were assigned according to the vertical fracture height growths from the horizontal well. These fractures were created in HydroGeoSphere deterministically by inputting individual fracture coordinates.

Table 3. Summary of Scenario Simulated

Scenarios	No. of Fractures	Upward Fracture Growth ^a (m)	Downward Fracture Growth ^a (m)	Fracture Length (m)	Fracture Aperture (μm)	Fracture Upward Growth Penetrating Geological Units (Fully/Partially)
A	6	200	200	400	200 ^b	–/BSF
B	6	400	400	800	200 ^b	BSF/MGG
C	6	950	400	1350	200 ^b	BSF, MGG/–
D	6	1000	400	1400	200 ^b	BSF, MGG, LCM/–
E	6	1300	400	1700	200 ^b	BSF, MGG, LCM, CS and MM/SBS
F	6	1850	400	2250	200 ^b	BSF, MGG, LCM, CS, MM, SBS/–
G	Same as those in Scenarios A, D, and F				20, 63, 1000 ^c	Same as those in Scenarios A, B, and F

^aReference to the horizontal well at $z = 750$ m.

^bEquivalent to hydraulic conductivity of $2.9 \times 10^{-2} \text{ m s}^{-1}$ according to the cubic law.

^cEquivalent to hydraulic conductivities of 2.9×10^{-4} , 2.9×10^{-3} , and $7.3 \times 10^{-1} \text{ m s}^{-1}$ each according to the cubic law, –: NA, MGG: Mercia Mudstone Group, SSG: Sherwood Sandstone Group, SBS: St. Bees Sandstone, MM: Manchester Marl, CS: Collyhurst Sandstone, LCM: Lower Coal Measures, MGG: Millstone Grit Group, and BSF: Bowland Shale Formation.

Six scenarios (Scenarios A–F) with different vertical fracture height growths induced by the fluid injection were used for the risk analysis associated with the vertical fracture growth. In addition, another scenario (Scenario G) was also employed to investigate the impact of the fracture aperture. All scenarios are summarized in Table 3, and described here. Scenario A examines a typical hydraulic fracturing scenario ($\sim 80\%$ probability), where upward and downward fracture growths from the horizontal well ($z = 750$ m) are less than 200 m. In this case, the propagated fractures are contained within the Bowland Shale, representing one of the best case scenarios. Scenario B represents $>99\%$ probability of the hydraulic fracturing scenarios, with 400 m each in upward and downward fracture growths. In this scenario, the fracture growths penetrate the Bowland Shale, and extend upward into the Millstone Grit Group 150 m and downward into the Pendleside Limestone 50 m. Scenarios C and D represent exceptional circumstances with 950 and 1000 m upward fracture growths, which are equivalent to the recorded fracture height of ~ 1000 m reported from offshore Nigeria [Loseth *et al.*, 2011]. The upward fracture growth in Scenario C penetrates the Bowland Shale formation, Millstone Grit Group and Lower Coal Measures. Scenario D extends Scenario C, with the upward fracture growth further penetrating the Collyhurst Sandstone.

Scenarios E and F represent two of the worst case scenarios where the upward fracture growth has been intercepted by the existing geological faults to create six fracture-fault conduits for the upward water and mass fluxes. These fracture interceptions are assumed to create 1300 and 1850 m interconnected upward fractures. The 1300 m fracture assumed in Scenario E extends Scenario D to further penetrate the overlying Manchester Marl. The 1850 m fracture growth in Scenario F penetrates all layers between the Bowland Shale and the Sherwood Sandstone, directly connecting these two layers directly by fractures. The existing seismic data indicated that there were several main faults within the Lancashire Bowland Shale license area, and a major fault with vertical displacement up to 1800 m lies largely within the Permian and Sherwood Sandstone Group [de Pater and Baisch, 2011]. Thus the interception between the upward hydraulic fracture growth and the existing faults within the license area could create extensive vertical fractures connecting the fractured shale with the overlying aquifers [The Royal Society and The Royal Academy of Engineering, 2012]. For Scenarios A–F, a constant fracture aperture of 200 μm was assigned for the fracture growth. This fracture aperture was assumed to be the typical aperture of the induced hydraulic fracture, according to the average of the proppant sizes (100–400 mesh: equivalent to the sieve sizes of 152–422 μm), which was used to support the fracture opening during hydraulic fracturing [Arthur *et al.*, 2008]. In addition to Scenarios A–F, Scenario G was used to examine the effect of fracture aperture on upward water and mass fluxes, by repeating simulations in Scenarios A, D, and F using fracture apertures of 20, 63, and 1000 μm , respectively.

3. Results and Discussions

3.1. Simulated Reference Scenario

The reference scenario here represents a base case before hydraulic fracturing. Thus, no fracture growths were considered in this scenario simulation. Due to the lack of information of hydraulic properties of the deep geological layers and boundary conditions, the intention was to generate a subjectively realistic hydrogeological model representing the Bowland Shale in Lancashire, UK. With the selected parameter

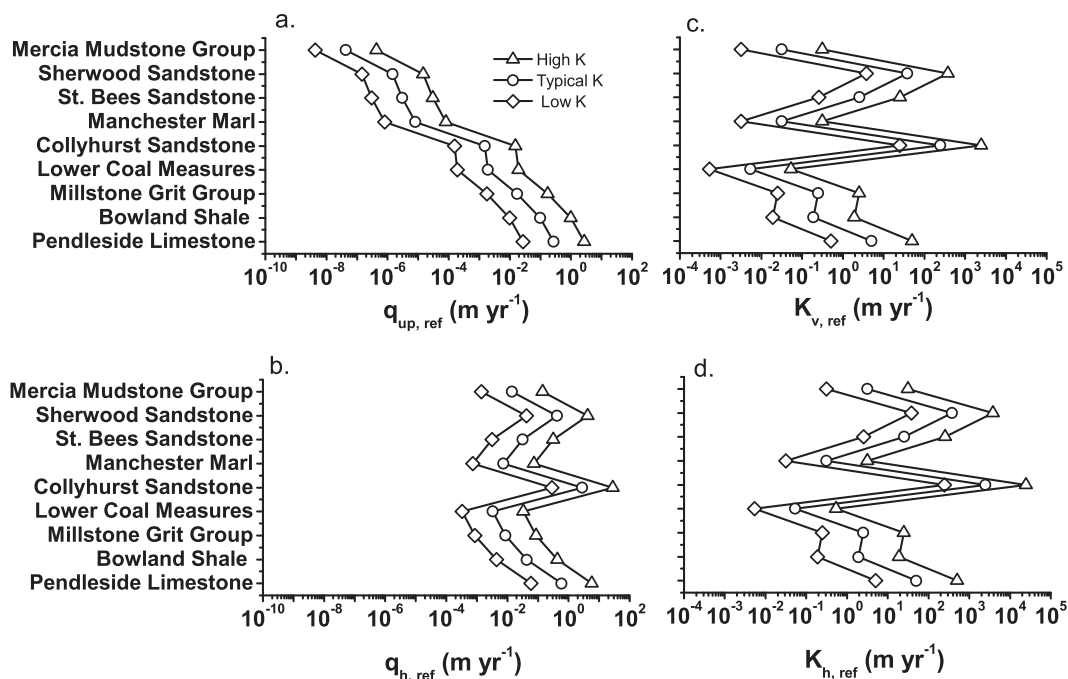


Figure 3. Steady-state water fluxes and hydraulic conductivities in pre-hydraulic fracturing conditions. (a) Upward water flux rates toward geological layers. (b) Horizontal water flux rates at $x=3300$ m within geological layers. (c and d) Vertical and horizontal hydraulic conductivities of geological layers.

values listed in Table 1, steady state flow simulations indicate that, under the assumed 250% upward gradient at the bottom of the domain, an average upward head gradient of 0.22 has been created within the Bowland Shale for three test K cases (supporting information Figure 1S). This upward gradient is similar to the estimated “effective” brine upward gradient of ~ 0.23 by considering heat (100°C), overpressure (20 MPa) as well as the density difference between fresh water and brine (density: 1230 kg m^{-3} and salinity: 350 g) within the shale formations [Flewelling and Sharma, 2014]. By using this flux boundary condition, the model can implicitly account for impacts of the overpressure, heat, and variable density on upward fluid and mass fluxes due to the lack of field observation data.

The result (Figure 3a) shows that the upward flux boundary condition does create vertical upward water fluxes toward overlying geological layers. The upward flux rate varies ~ 7 orders of magnitude in the multi-layered system for each K case tested, with the highest water flux rate at the bottom layer and the flux rate decreasing with the increase of the elevation. In addition, the upward water flux profile shows no clear correlation with the vertical hydraulic conductivity assigned for each geological layer (Figures 3a and 3c). While the horizontal water flux profile shows a clear correlation with the hydraulic conductivities assigned for each geological layer (Figures 3b–3d). Model results suggest that the upward water flux is severely intercepted by the high horizontal water flux rate within the Collyhurst Sandstone, with over 3 orders of magnitude of the reduction of the upward water flux (Figure 3a). This results in a low upward head gradient in the geological layers above (supporting information Figure 1S) leading to low upward water flux rates ($< 10^{-4}$ m/yr) toward the overlying Sherwood Sandstone aquifer layer. Overall, the upward head profile in the multi-layered system is similar to head profiles observed in two deep wells up to 1600 m depth at Sellafield, UK (~ 60 km north of the Lancashire Bowland Shale basin) [Littleboy, 1995; McKeown et al., 1999]. This suggests that the approximation of the upward water flux driven by heat and overpressure through assigning the upward flux boundary condition at the bottom of the domain would be an appropriate approach to represent the upward flux from the Bowland Shale.

With the selected solute transport parameters, chloride transport from the brine in the Bowland Shale and below (without hydraulic fracturing) was simulated for an 11,000 year period, with initial chloride concentrations of zero everywhere except the source zone. The resulting concentration profiles along the longitudinal section ($y = 1500$ m) at the end of 11,000 year simulation are presented in Figure 4. The chloride

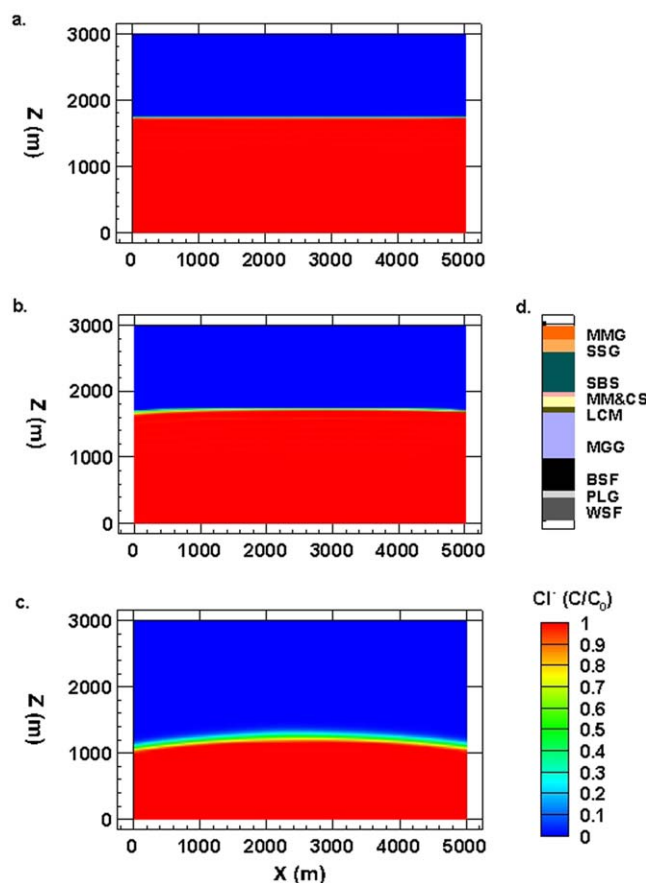


Figure 4. Chloride concentration profile along longitudinal section ($y = 1500$ m) at the end of the reference simulation (11,000 years). (a) High hydraulic conductivity case. (b) Typical hydraulic conductivity case. (c) Low hydraulic conductivity case. (d) Stratigraphic units over 3000 m depth: MMG-Mercia Mudstone Group, SSG-Sherwood Sandstone Group, MM-Manchester Marl, CS-Collyhurst Sandstone, LCM-Lower Coal Measures, MGG-Millstone Grit Group, BSF-Bowland Shale Formation, PLG-Pendleside Limestone Group, WSF-Worston Shale Formation.

concentration profile of the high K case shows that the upward mass flux from the Bowland Shale fully penetrates the geological layers below the Collyhurst Sandstone. The upward mass flux, however, appears to be limited to the Collyhurst Sandstone and below, as little change of chloride concentration profile is found in the multilayered system after 1000 year (Figure 4a and supporting information Figure 2Sa). This suggests that the upward mass flux is significantly intercepted by the high horizontal water fluxes within the Collyhurst Sandstone as indicated from the water flux analysis. The interception of the horizontal flux creates a steep salinity gradient (or saline transition zone) within the Collyhurst Sandstone. A similar zone with a steep salinity gradient was also reported at 300–400 m below ground surface level at Sellafeld, where some high permeability layers are located [Bath et al., 2006]. For the typical K case, the upward chloride flux enters the Millstone Grit Group about ~400 m after 1000 year (supporting information Figure 2Sb) and fully penetrates the geological layers below the Collyhurst Sandstone at the end of 11,000 years. Similar to the high K case, a steep salinity gradient within the Collyhurst Sandstone is found in the typical K case (Figure 4b).

For the low K case, chloride travels upward ~400 m into the Millstone Grit Group after the 11,000 year simulation (Figure 4c). By using the calculated upward water flux rate toward the Millstone Grit Group of ~0.002 m/yr (Figure 3a), advective chloride upward travel distances into the Millstone Grit Group shall be 220 m after 11,000 years. Higher simulated chloride travel distances suggest that the upward mass flux in Millstone Grit Group is significantly affected by diffusion transport. Despite the low upward mass flux rate in the low K case, the upward chloride flux is expected to fully penetrate the geological layers below the Collyhurst Sandstone layer, as those in the high and typical K cases, for longer simulation durations (e.g., 100,000 years). Due to the relatively high horizontal flux to the upward flux within the Collyhurst Sandstone, the upward chloride flux will be limited within the geological layer, creating a steep salinity gradient within the Collyhurst Sandstone as predicted in the high and typical K cases. Overall, the reference simulation suggests that, under prehydraulic fracturing conditions, contaminants from the Bowland Shale and below are unlikely to pose risks to groundwater within the overlying aquifers of the Sherwood Sandstone. This is due to the upward flux intercepted by the high horizontal flux rate within the Collyhurst Sandstone, which creates a high salinity gradient within the geological layer.

3.2. Simulated Fluid Injection and Pressure Release

Hydraulic fracturing involves the fluid injection of 9000–29,000 m³/well. This high pressure injection of the fracturing fluid will alter the preexisting steady state flow conditions, accompanying fracture propagations. The induced fracture will not only change flow pattern in the shale domain, but also provide new pathways

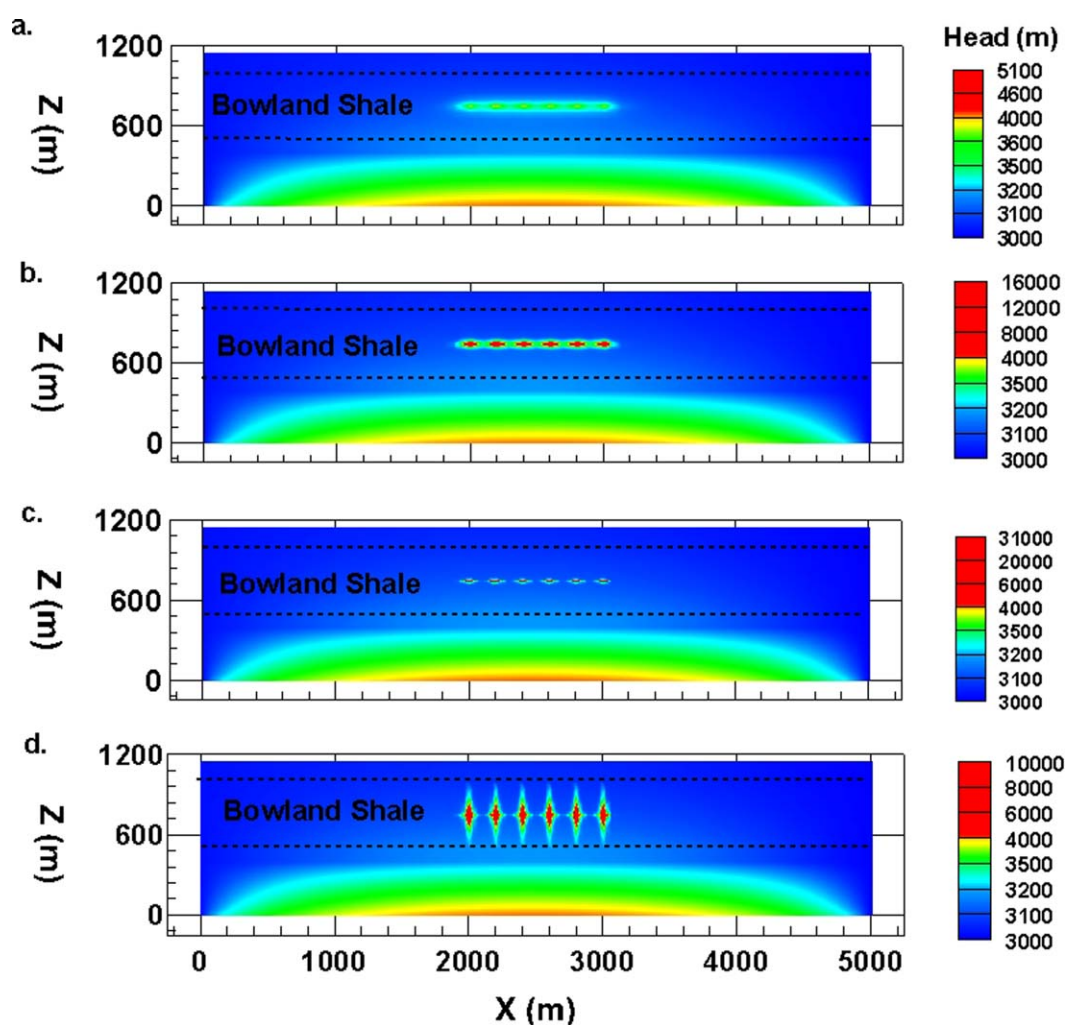


Figure 5. Hydraulic pressure head profile along longitudinal section ($y = 1500$ m) without fracture propagation (a–c) and with fracture propagation (d) during fluid injection. (a–c) After 2500 m^3 fluid injection: high K case (a), typical K case (b), low K case (c). (d) 200-m upward and downward fracture growths immediately after the 2500-m^3 fluid injection in low K low case followed by an additional 1250-m^3 fluid injection.

for solute transport within the deep bedrock system. Therefore, a better understanding of fluid flow during and after the injection processes provides key information for the long-term risk assessment of the hydraulically fractured shale. Figures 5a–5c show the pressure head distributions after the 2 h fluid injection of 2500 m^3 without the fracture propagation. The volume of fluid injection here is lower than the reported $9000\text{--}29,000\text{ m}^3/\text{well}$. This is because the typical fluid injection time of each fracture treatment was generally less than 2 h [e.g., Daneshy, 2010; de Pater and Baisch, 2011]. We simulate the six-stage hydraulic fracturing, with only one fracture treatment for each stage. Hydraulic fracturing in shale gas production can include up to 16 stages, with multifracture treatments for each stage. The results show that high pressure heads created by the fluid injection are mainly contained within the Bowland Shale. The magnitudes of the pressure heads, however, vary considerably for the three hydraulic conductivity cases, from the highest pressure head of ~ 5100 m for the high K case to $\sim 31,000$ m for the low K case at the end of the injection. Given that the steady state heads in the domain were about 3200 m within the Bowland Shale, this means that the 2 h injection created extrapressure heads of around 2000 , $13,000$, and $28,000$ m in the injection wells for the high, typical, and low K cases, respectively.

It is important to recognize that, due to the limitations of the model, the simulated fluid injection did not consider impacts of the rock deformation and the fracture growth. The fracture growth during the fluid

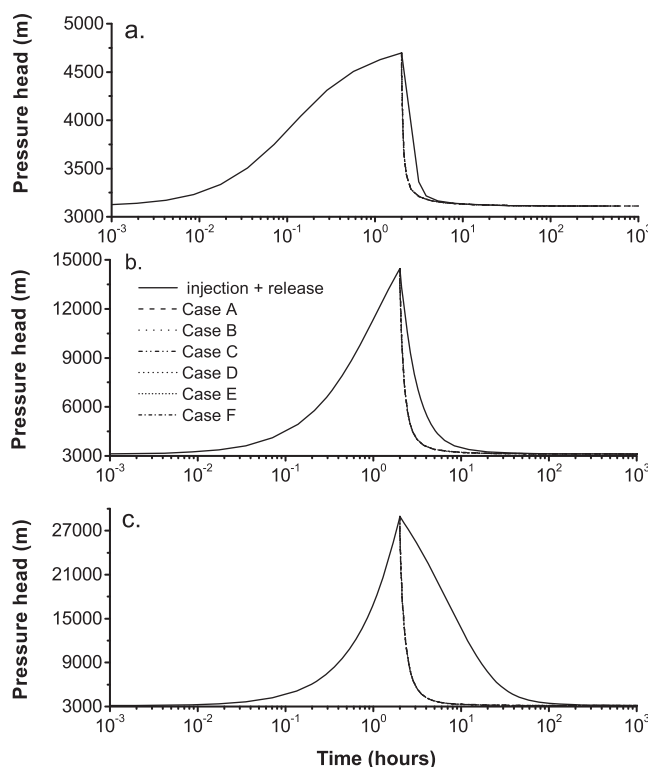


Figure 6. Hydraulic pressure heads in one injection well segment during and after the fluid injection. No fracture propagation assumed in the injection + release scenario. (a) High K case. (b) Typical K case. (c) Low K case.

place in the first few minutes of the injection, and no/slow increase of the pressure was observed afterward. This indicates that the fracture propagation likely starts after the first few minutes' fluid injection, as recorded seismic events were detected in this time frame of some Lancashire field operations [de Pater and Baisch, 2011]. Given that the model used for this study cannot accommodate the rock deformation and fracture propagation during the fluid injection, we only compare the first few minutes of simulated pressure head profiles against the field data. The impact of rock deformation and fracture propagations on the well pressure head is believed to be small in this time frame. The transient head profiles in one injection well (Figure 6) show that pressure head at the first 6 min of the injection are 3900, 4500, and 4600 m for the high, typical, and low K cases, respectively. These are equivalent to the pressure elevations of 700, 1300, and 1400 m for each K case. The well pressure elevations for the typical and low K cases are at the range of 1300–2000 m observed in the first few minutes of the field injection operation. This suggests that bulk hydraulic conductivity of the Bowland Shale before hydraulic fracturing would be similar to the low K cases (K_h : 6×10^{-9} m/s) or lower, if the compressibility of the shale formation is accounted for. This value is on the same order of magnitude as the reported permeability of Marcellus (permeability: 2×10^{-16} m² equivalent to a hydraulic conductivity of $\sim 1.7 \times 10^{-9}$ m/s) and Barnett Shales (permeability: $< 10^{-17}$ m²) [Montgomery et al., 2005; Gassiat et al., 2013]. Meanwhile, the elevation of the well pressure head (~ 1500 m, Figure 6a) at the end of 2 h injection for the high K case is similar to those in the field operation, suggesting that bulk hydraulic conductivity of the Bowland Shale after hydraulic fracturing is likely at the range of the high K case (K_h : 6×10^{-7} m/s), provided that the deformation of rocks does not have significant impact on the well pressure head estimation. These results are consistent with a report that hydraulic fracturing increased 100–1000 times of the permeability of shale formation [King, 2012].

The simulated pressure head releases after the cease of the injection were also carried out for the scenarios without fracture propagation and with fracture propagation of Scenarios A–F (Figure 6). The pressure head profiles indicate that the hydraulic conductivity and the upward fracture height growth have very limited impact on the pressure head release. It is evident that the pressure heads in the injection wells return the

injection would provide new hydraulic conduits for fluid flow, which can significantly reduce the pressure head within the injection well. In addition, the fluid flow within the fracture openness also increases the pressure head along the induced fracture, which would create a “4-point star” shape of the high pressure head distribution as demonstrated in an additional fluid injection simulation (Figure 5d). With the same injection rate as before, the additional simulation continues the fluid injection for another hour after the 2500 m³ fluid injection in the low K case.

The field operation in Lancashire reported that the injection created extra $\sim 13,000$ – $20,000$ kPa pressure (equivalent to ~ 1300 – 2000 m water pressure head) within the injection well. This elevation of the well pressure mainly took

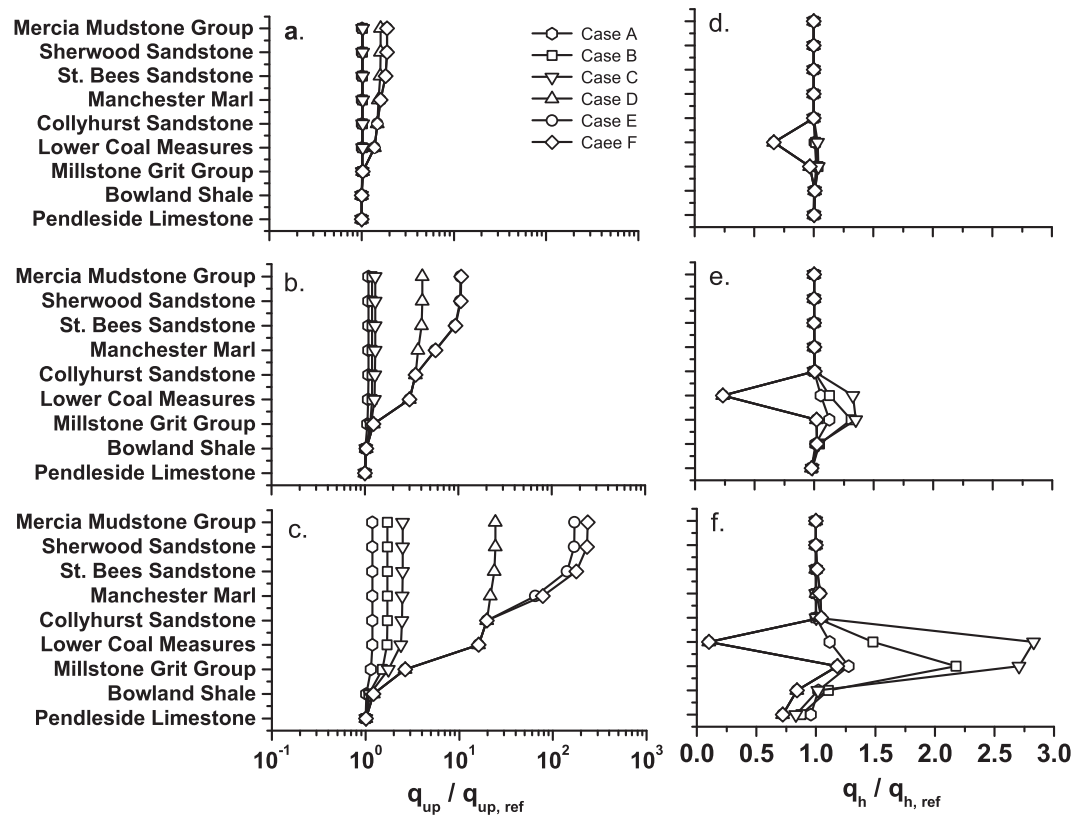


Figure 7. Effect of upward fracture height on water fluxes (Scenarios A–F). (a–c), Ratios of upward water flux towards geological layers after (q_{up}) and before hydraulic fracturing ($q_{up,ref}$), for the high (a), typical (b) and low (c) K cases. (d–f), Ratios of horizontal water flux at $x=3300$ m within geological layers after (q_h) and before ($q_{h,ref}$) hydraulic fracturing for the high (d), typical (d) and low (f) K cases.

preinjection levels for all test scenarios within 200 h after the cease of the injection. This is different to ~ 300 days reported by Myers [2012], suggesting that the boundary effect may have significant influence on Myers’s results as pointed out by Sayers and Barth [2012]. Our simulations of the pressure head profiles within the injection well after the cease of injection are similar to those reported in the Lancashire field operation, which exhibit a sharp decline of the pressure head immediately after the cease of the injection with a long tail [de Pater and Baisch, 2011]. However, we must stress that the intention of injection and pressure release simulations is not to reproduce the field injection operation, as the deformation of rocks and fracture propagation during the injection and pressure release could have significant impact on the pressure head within the rock system which the model cannot account for. Nevertheless, the simulation reveals that the transition flow caused by the fluid injection is short-lived and new steady state flow conditions are expected to establish with a matter of a couple of weeks after the cease of the fluid injection.

3.3. Impacts of Fracture Height on Water Fluxes (Scenarios A–F)

Once the hydraulic fracturing process has been performed in the shale formation, the preexisting flow conditions will be altered by the newly propagated fractures. These new fractures provide new conduits for water flow, and ultimately increase bulk hydraulic conductivity of the rock system. Impacts of these propagated fractures on fluid flow field depend on several factors, for example, the number of the fracture propagations, fracture height, connectivity and aperture, etc. Figure 7 shows the effect of the upward fracture height growth on water fluxes (Scenarios A–F). These effects are expressed as ratios of steady state water fluxes after and before hydraulic fracturing, i.e., $q_{up}/q_{up,ref}$ (upward flux ratio) and $q_h/q_{h,ref}$ (horizontal flux ratio). The simulations show that the water flux ratios vary from 0.1 to 200 over Scenarios A–F. Overall, the upward fracture height growth appears to have significant effect on the vertical water fluxes for the typical

and low K cases, particularly for the upper layers as the upward fluxes toward the Sherwood Sandstone and the St. Bees Sandstone increase over 2 orders of magnitude in some fracturing scenarios. With the horizontal flux ratios at a range of 0.1–3, impact of hydraulic fracturing on the horizontal water flux is, however, very limited. This impact is mainly within the layers below the Millstone Grit Group, which is unlikely to have significant effect on the upward solute transport.

Figure 7 shows that flux ratios are less than a factor of 3 for Scenarios A–C, suggesting that upward fracture growths in these scenarios have very limited effects on water fluxes. It is particular for the high and typical K cases as little/no changes in water flux rates (Figures 7a–7d). This is due to the fact that the upward fracture growths in Scenarios A–C, with an aperture of 200 μm within the Bowland Shale and the Millstone Grit Group, have limited effects on bulk hydraulic conductivities of the rocks within these two layers. For the low K cases, the fracture growths do have a stronger impact on bulk hydraulic conductivities of the host rocks due to the bigger contrast between the hydraulic conductivities of the prehydraulic fracturing rocks and open fractures. This leads to some increases of the upward flux rates up to ~ 3 times toward the Lower Coal Measures and above. Meanwhile, increases of the horizontal water flux rates within the Millstone Grit Sandstone and the Lower Coal Measures (Figures 7e and 7f) suggest some of the increased upward water flows are diverted to the horizontal flow within these two geological layers, preventing substantial increases of the upward fluxes. This is a result of the low vertical permeability of the Lower Coal Measures which acts as an impermeable barrier to prevent further upward flow. The simulations from Scenario D appear to prove this point, as significant increases of upward water fluxes up to 20 times are observed for the low K case, once the 50 m thick Lower Coal Measures has been fully penetrated by induced fractures (Figure 7c). The simulations also show that the water flux via induced fractures within the Lower Coal Measures contributes a significant amount ($>99\%$) of the total upward water flow in the low K case. With the increase of the upward water flux through the impermeable Lower Coal Measures, the horizontal water flux within the Lower Coal Measures reduces to $\sim 10\%$ of the reference case, but little changes are found above the layer (Figure 7f). For the high and typical K cases, similar water flux patterns as those in the low K case are observed, but impacts of the upward growth on the upward and horizontal flux rates are much smaller (Figures 7a, 7b, 7d, and 7e). The simulations show that the water flux via induced fractures within the Lower Coal Measures, unlike that in the Low K case, just contributes $\sim 8\%$ of the total upward flux in the high K case, and 50% in the typical K case. This is due to the fact that the upward water flux via matrix rocks also contributes a certain amount of total upward water flow, as the differences between the hydraulic conductivities of the rock matrix and open fractures are not that significant as those in the low K case.

For the Scenario E, the penetration of the low permeable layer of the Manchester Marl by induced fractures does lead to a significant increase of the upward water flux toward the Manchester Marl and above, with a magnitude of ~ 1 order for the low K case compared with Scenario D. Impacts of the upward fracture growth in the Manchester Marl are, however, far less significant in the high and typical K cases. Little/no changes in the water fluxes are found to the high K case compared with Scenario D, while a further increase of the upward flux to ~ 10 times of the reference case is found for the typical K case. The further upward fracture growth of Scenario F only shows a slight increase of the upward water flux toward the Manchester Marl and above for the low K case. The rest remains unchanged as those in Scenario E, despite the upward fracture growth with an aperture of 200 μm directly connecting the Bowland Shale and the overlying Sherwood Sandstone aquifer. Overall, the simulations suggest that upward fracture growths penetrating the low permeable layers of the Lower Coal Measures and the Manchester Marl would substantially increase the upward water fluxes toward the overlying aquifers of the St. Bees Sandstone and the Sherwood Sandstone up to ~ 200 times in the low K case and ~ 10 times in the typical K case, but < 2 times in the high K case.

3.4. Impacts of Fracture Height on Mass Fluxes

As expected, upward fracture growths induced by hydraulic fracturing can alter the preexisting flow field in the bedrock system. The scale and magnitude of this impact relative to fracture height growths and hydraulic conductivity of the multilayered geological system has been analyzed above. Unlike the water flow, solute transport in fractured rock is, however, rather complicated. Mass flux in such a system is not only controlled by water flux rates as those in porous media, but also affected by mass exchange between the fractures and the host rock. This solute transport phenomenon is often regarded as “dual-porosity” transport when the permeability of the fracture is much higher than the host rock. In this case, mass flux via water

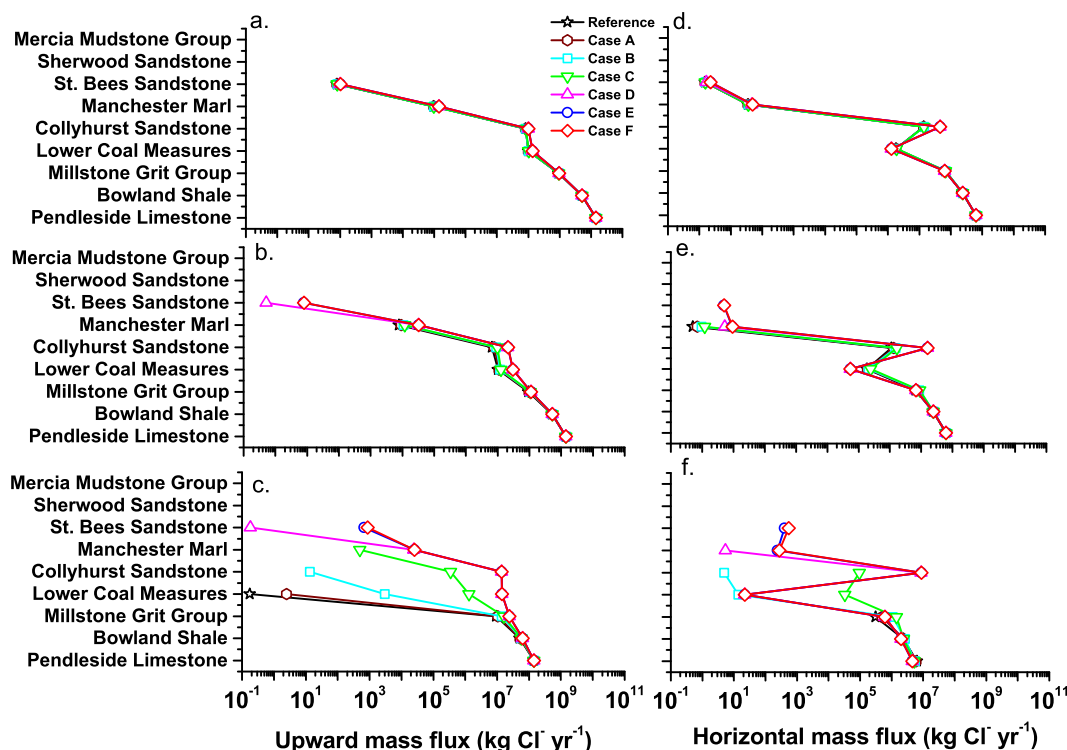


Figure 8. Effect of upward fracture height on mass fluxes (Scenarios A–F). (a–c). Upward mass flux toward geological layers without (Reference) and with hydraulic fracturing (Cases A–F) for the high (a), typical (b) and low (c) K cases. (d–f), Horizontal water flux at $x=3300$ m within the geological layers before and after hydraulic fracturing for the high (d), typical (e) and low (f) K cases.

flow in the host rock is negligible and solute transport in the rock matrix is dominated by diffusion transport. Mass diffusion from the fracture into the rock matrix often acts as “source sink” in the fracture. Modeling of solute transport in such a fractured rock often requires a discrete fracture system where the fracture network is represented explicitly in the rock matrix. In the cases where the hydraulic conductivities of the fracture and the host rock are not significant, solute transport in the fractured system can be treated as that in porous media (often called as “equivalent porous media”). Mass exchange between the fracture and the host rock are presented by dispersive transport. In this study, the geological layers before hydraulic fracturing are represented by equivalent porous media due to the lack of information of initial fracture network system. Upward fracture growths for the hydraulic fracturing scenarios are, however, represented explicitly in the model domain. Given that the hydraulic conductivities of the multilayered system span 5 orders of magnitude in the scenarios tested, solute transport in these bedrock layers will vary considerably.

3.4.1. Typical Upward Fracture Growth Scenarios (Scenarios A and B)

Figure 8 shows the vertical upward and horizontal mass fluxes with and without hydraulic fracturing. Note that mass flux rates with hydraulic fracturing presented here are the flux rates at the end of the 10,000 year simulation, with starting concentrations of the year 1000 of the reference simulation (without hydraulic fracturing). This means that the total simulation time for the fracturing scenarios is 11,000 years when including the 1000 year prefracturing simulation. Mass flux rates for the reference scenario presented here are those rates at the end of 11,000 year continuing simulation without hydraulic fracturing. Transient upward mass flux profiles show that upward flux rates at the end of the 11,000 years are maximum fluxes, despite the fact that the pressure built-up during the fluid injection has some impacts on the upward mass flux rate toward the Millstone Grit Group. However, these impacts are negligible and short-lived (supporting information Figure 3S), which was confirmed by the pressure head release simulations (Figure 6). All flux rates were calculated by using a constant released concentration of $350 \text{ g Cl}^-/\text{L}$ in the source zone [Warner *et al.*, 2012; Flewelling and Sharma, 2014]. The simulations indicate that upward fracture growths in Scenarios A and B have little impacts on overall chloride mass fluxes in the fractured rock system. The results show that upward and horizontal flux rates in these two scenarios, except the low K case in Scenario B, are either

below $0.1 \text{ kg Cl}^-/\text{yr}$ or identical to those of the reference scenario (Figure 8). There are, however, some small increases of the upward mass fluxes toward the Collyhurst Sandstone and the Lower Coal Measures in the low K case of Scenario B, as well as the horizontal fluxes. However, none of these has impacts on mass fluxes within the Manchester Marl and above. The chloride concentration profiles along the longitudinal section, at which the horizontal well is located ($y = 1500 \text{ m}$), after 10,000 years hydraulic fracturing show little differences between Scenario A and the reference scenario (supporting information Figure 4S and Figure 4). However, the concentration profiles reveal that the upward fracture growth in Scenario B does provide some pathways for chloride upward transport into the Millstone Grit Group, significantly increasing chloride concentrations in some areas near induced fractures of the Millstone Grit Group for the low K case (supporting information Figure 5Sc). Overall, the results suggested both upward fracture growth scenarios of $\leq 200 \text{ m}$ (Scenario A: 80% probability) and $\leq 400 \text{ m}$ (Scenario B: 99% probability) have negligible impacts on the upward chloride mass fluxes, which is unlikely to pose a risk to the water quality in the geological layer above the St. Bees Sandstone.

3.4.2. Exceptional Upward Fracture Growth Scenarios (Scenarios C and D)

For Scenarios C and D, hydraulic fracturing results in upward vertical fracture growths of 950 and 1000 m, which is similar to the recorded upward height of the induced fracture in offshore Nigeria [Loseth *et al.*, 2011]. The simulations (Figure 8) suggest that the full penetration of the Millstone Grit Group by induced fractures of Scenario C does result in some increases of upward mass fluxes in the low K case, while have negligible impacts in both upward and horizontal mass fluxes for the high and typical K cases. This is because water flux in fractures contributes significant amount of total upward water flux in the low permeability host rock case, which is consistent with the results from the water flux analysis (Figure 7). In addition, the low permeability of the host rock also reduces the mass flux rate from the fractures into the rock matrix by diffusion, sustaining mass upward flux via induced upward fractures. For the low K case, the upward mass flux rate increases ~ 2.5 orders of magnitude to over $1 \times 10^6 \text{ kg Cl}^-/\text{yr}$ toward the Lower Coal Measures, ~ 4.5 orders to $3 \times 10^5 \text{ kg Cl}^-/\text{yr}$ toward the Collyhurst Sandstone, and from below $0.1 \text{ kg Cl}^-/\text{yr}$ to $5 \times 10^2 \text{ kg Cl}^-/\text{yr}$ toward the Manchester Marl (Figure 8c). Meanwhile, the horizontal mass fluxes within the Lower Coal Measures and the Collyhurst Sandstone also increases about 4–5 orders of magnitude to the levels close to their upward flux rates (Figures 8c and 8f). The elevated horizontal mass flux rate within the Collyhurst Sandstone leads to a sharp decline (~ 3 orders of magnitude) of the upward mass toward the Manchester Marl from the layer. This suggests that the upward mass flux is significantly intercepted by the high water flux rate within the Collyhurst Sandstone, diverting the upward mass flux to the horizontal flux and significantly reducing the upward mass flux. Overall, mass fluxes and longitudinal concentration profiles (Figure 8 and supporting information Figure 6S) show that the impact of the upward fracture growth in Scenario C is limited to the Collyhurst Sandstone and below. This suggests that the increase of the upward mass flux is unlikely to pose risks to the overlying groundwater quality within St. Bees Sandstone and above.

For Scenario D, the upward fracture growth extends 50 m further upward to fully penetrate the overlying impermeable layer of the Lower Coal Measures. The results (Figure 8) suggest that, similar to Scenario C, the upward fracture growth has negligible impacts in both upward and horizontal mass fluxes in the high K case. For the typical and low K cases, the penetration of the Lower Coal Measures by induced fractures does increase upward mass fluxes toward the geological layers between the Collyhurst Sandstone and St. Bees Sandstone. The magnitude, however, varied considerably in these two K cases, with higher impact up to 2 orders of magnitude for the low K case. Overall the impact of the upward fracture growth on the upward fluxes limits to the St. Bees Sandstone and below, as the maximum upward mass flux rates are below $1 \text{ kg Cl}^-/\text{yr}$ toward the St. Bees Sandstone in both K cases. Meanwhile, the upward fracture growth appears to have some influences on the horizontal mass fluxes, particularly for the typical and low K cases. For the typical K, there is a slight decline of the horizontal mass flux within the Lower Coal Measures, but an increase up to 1 order of magnitude within the Collyhurst Sandstone. For the low K case, the upward fracture growth has more significant impact on the horizontal mass flux than those in the typical case. There is a substantial decrease of the horizontal mass flux within the Lower Coal Measures up to 3 orders of magnitude, while an increase up to 2 orders of magnitude within the Collyhurst Sandstone (Figures 8e and 8f). The impact of the horizontal mass flux by the upward fracture growth in the typical and low K cases is a result of the increase of the upward mass flux from the Lower Coal Measures via the induced fractures, as model results indicate 50% and 99% of upward mass fluxes via induced fractures in the both K cases, respectively. Meanwhile,

induced fractures within the Lower Coal Measures also divert the horizontal flux upgradient into the vertical fluxes. This results in the reduction of the horizontal mass fluxes within the Lower Coal Measures, which is consistent with the result from the water flux analysis (Figure 7). Similar to Scenario C, the increase of the upward mass flux from the Lower Coal Measures appears to be significantly intercepted by the horizontal flows within the Collyhurst Sandstone, which results in the elevation of the horizontal mass fluxes (Figures 8e and 8f). The longitudinal chloride concentration profile in the low K case clearly demonstrates that the horizontal mass flux creates a chloride plume within the Collyhurst Sandstone (supporting information Figure 7Sc).

In all three K cases of Scenario D, horizontal mass fluxes within the high permeable layer of the Collyhurst Sandstone are the most significant of all, suggesting that a big proportion of the upward mass flux entering into the geological layer diverts into the horizontal flux. As a result of this, upward mass fluxes toward its overlying layer of the Manchester Marl reduce to a level less than ~ 3 orders of magnitude of those toward the Collyhurst Sandstone (Figure 8). With the low permeability of the Manchester Marl acting as an impermeable layer to prevent the further vertical upward flux, chloride upward mass flux to its overlying layers of the St. Bees sandstone become very small and below $1 \text{ kg Cl}^-/\text{yr}$ in the typical and low K cases (Figures 8b and 8c). The chloride concentration profiles and upward mass fluxes confirm that the impact of the fracture growth into the Lower Coal Measures of Scenario D on the upward mass flux is limited to the Manchester Marl and below, with no potential risk to the overlying Sherwood Sandstone aquifers.

3.4.3. Extreme Upward Fracture Growth Scenarios (Scenarios E and F)

Scenarios E and F look at some extreme rare cases where the vertical upward fracture growth intercepted by the existing natural fractures or faults creates six interconnected fractures. These fracture growths create 1300 and 1850 m interconnected upward fractures, which are assumed to provide hydraulic conduits to directly connect the upward flow and mass movement from the Bowland Shale to the St. Bees Sandstone (Scenario E), and to the overlying Sherwood Sandstone (Scenario F). We recognize that the geological faults would act as complex conduit-barrier systems [e.g., *Bense et al.*, 2013]. However, as the worst case scenarios in this assessment, the geological faults are assumed to act as a hydraulic conduit system only. With a mean fracture aperture of $200 \mu\text{m}$ applied for this analysis, this means that the permeability of the fault above the Bowland Shale was equivalent to $3.3 \times 10^{-9} \text{ m}^2$ (Hydraulic conductivity: $2.9 \times 10^{-2} \text{ m/s}$, Table 3). This is several orders of magnitude higher than the reported value of $10^{-15} - 10^{-11} \text{ m}^2$ for the fault above the shale formations in North America [*Gassiat et al.*, 2013]. In addition, theoretical studies and computer simulations of fracture-fault interactions suggested that hydraulic fracturing was unlikely to reactivate the existing fault zones [e.g., *Shapiro et al.*, 2011; *Flewelling et al.*, 2013; *Rutqvist et al.*, 2013]. This means that hydraulic fracturing shall have no influence on the permeability of the existing fault. Therefore, with the fracture aperture of $200 \mu\text{m}$, Scenarios E and F here may imply the reactivation of the existing fault by hydraulic fracturing. Thus, these two scenarios represent the extremely rare worst-cases in this assessment.

The results from Scenarios E and F (Figure 8) show that upward and horizontal mass flux rates in these two scenarios are almost identical (flux rates overlapped each other). This suggests that the further 650 m upward fracture growth with a mean aperture of $200 \mu\text{m}$ of Scenario F, which fully penetrate the St. Bees Sandstone, has little impact on mass fluxes when comparing with those in Scenario E. In addition to this, upward mass flux rates in Scenarios E and F within the Manchester Marl flux and below are identical to those in Scenario D (Figure 8). This suggests that the further upward fracture growths above the Collyhurst Sandstone have no impacts on upward mass fluxes within and below the Manchester Marl, which is consistent with the results from the water flux rate analysis (Figure 7). For the typical and low K cases, the upward fracture growths do have some impacts on the upward mass fluxes toward the St. Bees Sandstone, with increasing the mass flux rate from below 0.1 to $10 \text{ kg Cl}^-/\text{yr}$ in the typical K case and to $8 \times 10^2 \text{ kg Cl}^-/\text{yr}$ in the low K case. While the elevation of the upward mass flux is limited to the St. Bees Sandstone, as the impact of the upward mass fluxes toward the Sherwood Sandstone and above are negligible ($<0.1 \text{ kg Cl}^-/\text{yr}$).

The model results (Figures 8e and 8f) also show some elevations of horizontal mass fluxes within the Manchester Marl and the St. Bees Sandstone in both typical and low K cases. For the typical K case, the horizontal mass flux rate increases ~ 1 order of magnitude to $10 \text{ kg Cl}^-/\text{yr}$ within the Manchester Marl, and from below $0.1 \text{ kg Cl}^-/\text{yr}$ to 5 kg Cl^- within the St. Bees Sandstone. For the lower K case, the horizontal mass flux rate within the St. Bees Sandstone increases from below 0.1 to $\sim 500 \text{ kg Cl}^-/\text{yr}$, which is at a similar level to the upward mass flux rate ($\sim 800 \text{ kg Cl}^-/\text{yr}$) toward the geological layer. With a big proportion ($\sim 60\%$) of

the upward mass flux diverted to the horizontal flux and mass diffusion into thick rock matrix within the St. Bees Sandstone, the upward mass flux toward the Sherwood Sandstone becomes very small and negligible ($<0.1 \text{ kg Cl}^-/\text{yr}$). With the upward mass flux rate toward the Sherwood Sandstone below $0.1 \text{ kg Cl}^-/\text{yr}$ in all three K cases, the upward fracture growths in Scenarios E and F are unlikely to pose a risk to groundwater quality in the Sherwood Sandstone which is also demonstrated by the concentration profiles (supporting information Figures 8S and 9S).

3.5. Impacts of Fracture Aperture on Upward Fluxes (Scenario G)

In the above, the impact of the upward fracture height growth on water and mass fluxes in the multilayered geological system was analyzed. However, these analyses were carried out with a constant mean fracture aperture of $200 \mu\text{m}$ only. Water and mass fluxes within the multilayered system may not only be affected by the upward fracture height, the aperture of induced fractures would also have significant impacts on fluxes. Fracture aperture is considered as a key parameter representing the fracture permeability [Bear, 1972], which controls fluid flow and mass movement within the fracture openness. Due to the fact that there is very limited information on the induced fracture apertures by hydraulic fracturing, we conducted nine sets of simulations with the fracture apertures of 20, 63, and $1000 \mu\text{m}$ in Scenario G (Table 3). These simulations were carried out by assigning these aperture values to replace the original fracture apertures in Scenarios A, D, and F, given that water and mass fluxes in these three scenarios have showed distinguishing patterns with regards to the fracture height growths. As a result, four fracture aperture values (20, 63, 200, and $1000 \mu\text{m}$) were applied to investigate the impact of the induced fracture aperture on water and mass fluxes. According to the cubic law [Bear, 1972], the associated hydraulic conductivities of these four apertures are estimated to be 2.9×10^{-4} , 2.9×10^{-3} , 2.9×10^{-2} , and $7.3 \times 10^{-1} \text{ m/s}$ (Table 3). These hydraulic conductivities are equivalent to the permeability of 3.3×10^{-11} , 3.3×10^{-10} , 3.3×10^{-9} , and $8.3 \times 10^{-8} \text{ m}^{-2}$, respectively. This means that the permeability of the fracture apertures of $\geq 63 \mu\text{m}$ is much higher than the reported permeability (10^{-15} – 10^{-11} m^2) of the geological fault above the shale formations [Gassiat *et al.*, 2013]. Given that the upward fracture growth in Scenario F considers the case where induced fractures by hydraulic fracturing is intercepted by the existing faults, a mean fracture aperture $\geq 63 \mu\text{m}$ assigned for Scenario F may imply that the reactivation of the faults occurs during hydraulic fracturing. This is dismissed by several past studies [e.g., Shapiro *et al.*, 2011; Flewelling *et al.*, 2013; Rutqvist *et al.*, 2013]. Nevertheless, these scenarios represent some extremely rare cases in this risk assessment. To distinguish these three sets of simulations in Scenario G to the previous simulations, we group the four different apertures (20, 63, and $1000 \mu\text{m}$ as well as $200 \mu\text{m}$ from previous simulations of Scenarios A, D, and F) of the upward fracture growth into three subgroups, and name them as Scenarios G_A , G_D , and G_F , respectively.

3.5.1. Impact on Upward Water Flux

Figure 9 shows the effect of the fracture aperture on the upward water flux in the multilayered geological system. Again, these effects are expressed as ratios of steady state water fluxes after and before hydraulic fracturing. The results show that, with a fracture aperture $\leq 1000 \mu\text{m}$, the upward fracture height growth of 200 m ($\sim 80\%$ probability) in Scenario G_A has negligible impact on the upward water flux in all three K cases (Figures 9a–9c). For the upward fracture growth equivalent to the recorded height of 1000 m in Scenario G_D which fully penetrates the low permeability of the Lower Coal Measure, the induced fracture aperture does have some effects on the upward water flux. The magnitude of the effect increases with the decrease of the hydraulic conductivity (Figures 9d–9f), which is similar to the previous scenarios. For the aperture of $1000 \mu\text{m}$, the results show the upward water flux toward the Lower Coal Measures and above increase 30 to over 100 times of the prehydraulic fracturing conditions. For the fracture apertures of $200 \mu\text{m}$ and below, impacts of the fracture aperture are limited ($<$ a factor of 4) for all K cases tested, except a high impact (a factor of over 20) found in the low K case.

For Scenario G_F where the upward fracture growth directly connects the Bowland Shale and the overlying Sherwood Sandstone aquifer, the penetration of the low permeable Manchester Marl further increases the upward water flux toward the Manchester Marl and above as suggested in Scenarios E and F, but the magnitude varied significantly for the four apertures across the three K cases. For the high K case, impacts of the fracture aperture of $200 \mu\text{m}$ and below are rather small ($<$ a factor of 2). But a significant impact is found for the fracture aperture of $1000 \mu\text{m}$ with a factor of up to 300 (Figure 9g). For the typical K case, the increase of the fracture aperture on the upward water fluxes toward the Manchester Marl and above appears to be more significant than those in the high K case, from a factor of <2 to over 10 for the fracture

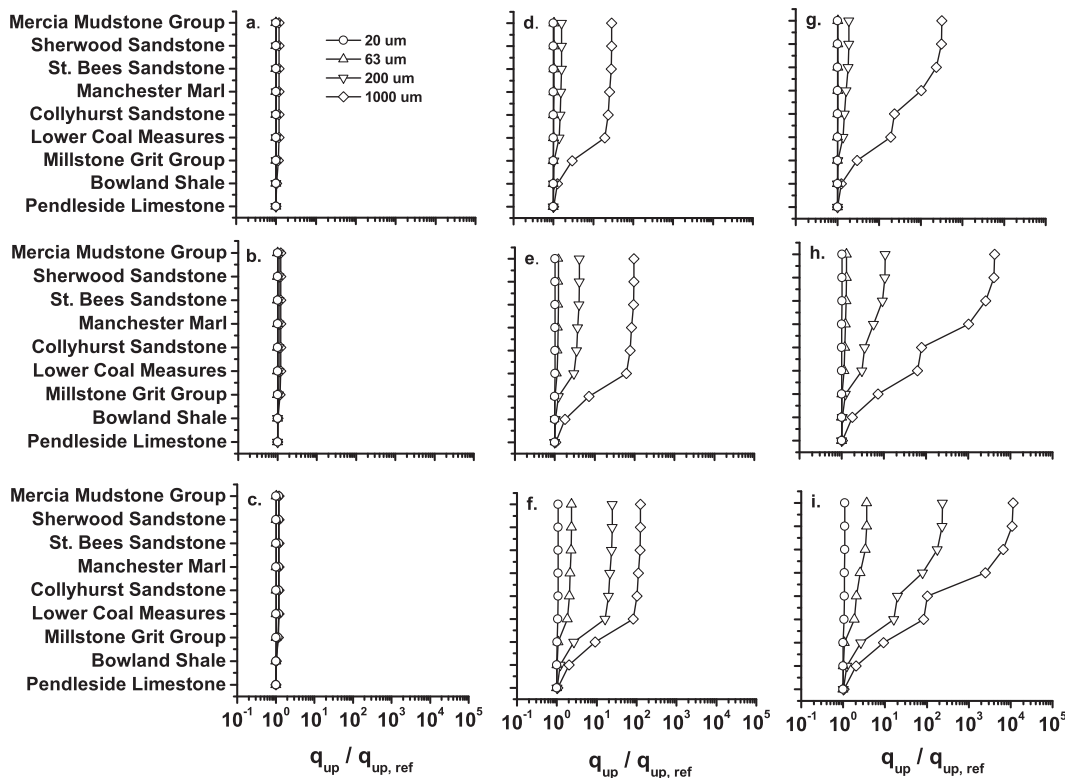


Figure 9. Effect of fracture aperture on upward water fluxes. Left column (a–c): Scenario G_A -upward fracture height growth in Scenario A. Middle column (d–f): Scenario G_D -upward fracture height growth in Scenario D. Right column (g–i): Scenario G_F -upward fracture height growth in Scenario F. Top panel (a, d, and g): high K case. Middle panel (b, e, and h): typical K case. Bottom panel (c, f, and i): low K case.

of 200 μm , and from a factor of 200 to over 4000 for the aperture of 1000 μm . However, little changes of upward water flux profiles are found for the cases with the apertures of 63 and 20 μm (Figure 9h). For the low K case, higher impacts than those in the typical K case are found in both apertures of 200 and 1000 μm . The upward water fluxes toward the Manchester Marl and above increase from a factor of ~ 10 to over 200 for the aperture of 200 μm , and from a factor of ~ 4000 to over 11,000 for the aperture of 1000 μm . Impacts for the apertures of 20 and 63 μm are less than a factor of 2 (Figure 9i). Overall, the results suggest that, with an induced fracture aperture $\leq 1000 \mu\text{m}$, upward fracture growth in Scenario G_A has no impact on overall upward water flux in the multilayered system. With an aperture $\geq 200 \mu\text{m}$, the upward fracture growth does have some effect on the upward water flux in Scenarios G_D and G_F . The magnitude varied considerably with the induced fracture height and the hydraulic property of the multilayered system. The highest impact is in the low K of the Scenario G_F with the aperture of 1000 μm , where the upward toward the overlying Sherwood Sandstone increases over a factor of over 11,000.

3.5.2. Impact on Upward Mass Flux

Figure 10 shows the upward mass flux with induced fracture apertures of 20, 63, 200, and 1000 μm , as well as without hydraulic fracturing. Again, mass flux rates were calculated by using a constant released concentration of 350 g Cl^-/L in the source zone at the end of the total simulation duration of the 11,000 years. As expected, the mass flux rate in Scenario G_A has no impact from the induced fracture apertures $\leq 1000 \mu\text{m}$ (Figures 10a–10c), which is consistent with the upward water flux (Figures 9a–9c). For Scenario G_D , overall upward mass flux is not sensitive to the fracture aperture $\leq 200 \mu\text{m}$ for the high and typical K cases. However, the increase of the fracture aperture to 1000 μm does increase the overall upward mass flux, with the upward mass flux toward the St. Bees Sandstone increased from 10^2 to 10^4 kg Cl^-/yr in both K cases (Figures 10d and 10e). For the low K case, fracture apertures of 20, 63, 200, and 1000 μm show distinguishing upward mass flux profiles (Figure 10f). This suggests that the upward mass flux is sensitive to the induced fracture aperture, which is also indicated by the upward water flux (Figure 9f). In general, the upward mass flux in Scenario G_D (Figures 10d–10f) shows a significant decline up to 11 orders of magnitude within the

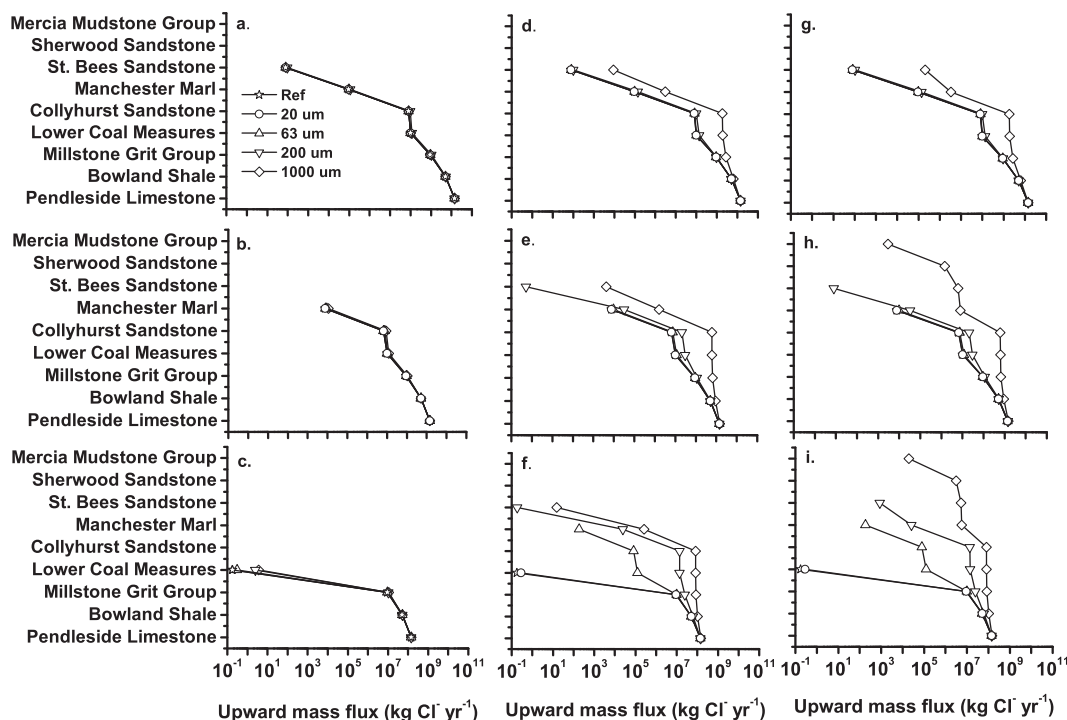


Figure 10. Effect of fracture aperture on upward mass fluxes. Left column (a–c): Scenario G_A —upward fracture height growth in Scenario A. Middle column (d–f): Scenario G_D —upward fracture height growth in Scenario D. Right column (g–i): Scenario G_F —upward fracture height growth in Scenario F. Top panel (a, d, and g): high K case. Middle panel (b, d, and h): typical K case. Bottom panel (c, f, and i): low K case.

geological layers between the Collyhurst Sandstone and St. Bees Sandstone, resulting in the upward mass flux rate to the overlying Sherwood Sandstone below $0.1 \text{ kg Cl}^-/\text{yr}$. This suggests that upward mass fluxes within these layers are significantly intercepted by the horizontal mass flux. Overall, results from Scenario G_D suggest that the increase of fracture aperture up to $1000 \mu\text{m}$ of the upward fracture height growth of 1000 m is unlikely to pose a risk to the overlying Sherwood Sandstone aquifer.

For Scenario G_F , the upward mass flux is, similar to Scenario G_D , not sensitive to the fracture aperture $\leq 200 \mu\text{m}$ in the high and typical K cases, but becomes very sensitive to the cases of the fracture aperture $\geq 1000 \mu\text{m}$. For the low K case, the upward mass flux is sensitive to all fracture apertures tested (Figures 10g–10i). With an increase of the fracture aperture from 200 to $1000 \mu\text{m}$ in the high K case, the upward mass flux toward the St. Bees Sandstone increases to $10^5 \text{ kg Cl}^-/\text{yr}$ from $10^3 \text{ kg Cl}^-/\text{yr}$. This increase is, however, limited to the St. Bees Sandstone and below, as the mass flux toward the Sherwood Sandstone aquifer is below $0.1 \text{ kg Cl}^-/\text{yr}$. This is due to the horizontal mass flux within the St. Bees Sandstone (supporting information Figure 10Sa). Despite the low upward mass flux rate ($\sim 10^{-3} \text{ kg Cl}^-/\text{yr}$) toward the Sherwood Sandstone aquifer in the high K case, the upward fracture growth with an aperture of $1000 \mu\text{m}$ in this scenario reduces the chloride travel time toward the Sherwood Sandstone from over $10,000$ to ~ 300 years (Figure 11a). For the typical K case, the increase of the fracture aperture to $1000 \mu\text{m}$ results in substantial increases of upward mass fluxes to the Millstone Grit Group and above. With an upward mass flux rate toward the Sherwood Sandstone elevated to over $10^6 \text{ kg Cl}^-/\text{yr}$ from below $0.1 \text{ kg Cl}^-/\text{yr}$ (Figures 10h), this creates a high concentration of chloride horizontal plume within the St. Bees Sandstone (supporting information Figure 10Sb), potentially posing a risk to groundwater in the Sherwood Sandstone aquifer. In addition, chloride travel time toward the overlying Sherwood Sandstone aquifer reduces to 100 years from the original over $10,000$ years (Figure 11b).

For the low K case of Scenario G_F , the induced fracture aperture significantly increases the overall upward mass flux for four fracture aperture tested (Figure 10i). With an upward mass flux rate to the overlying Sherwood Sandstone aquifer below $0.1 \text{ kg Cl}^-/\text{yr}$ for the fracture aperture $\leq 200 \mu\text{m}$ in all three K cases, the

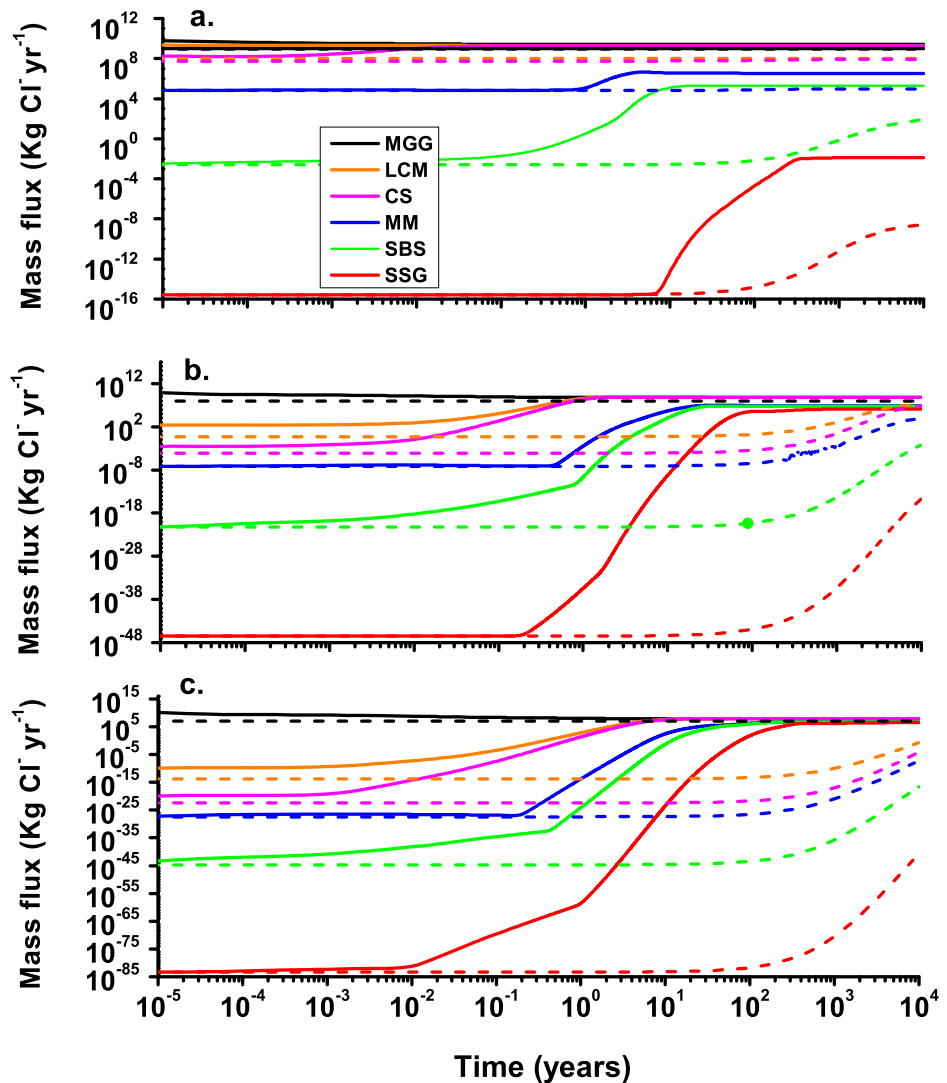


Figure 11. Chloride upward mass fluxes vs. time from years 1000 to 11000 for the Scenario G_p with fracture aperture of $1000 \mu\text{m}$ (one set of Scenario G_p) and the reference scenario. Solid line: Scenario G_p . Dash line: Reference scenario. (a) High hydraulic conductivity case. (b) Typical hydraulic conductivity case. (c) Low hydraulic conductivity case. MGG-Millstone Grit Group, LCM-Lower Coal Measures, MM-Manchester Marl, CS-Collyhurst Sandstone, SBS-St. Bees Sandstone and SSG-Sherwood Sandstone Group.

upward fracture growth is unlikely to pose a risk to the aquifer layer. For the extremely rare cases of the fracture aperture $\geq 1000 \mu\text{m}$, the upward mass flux is, however, very likely to pose significant threats to the groundwater quality. With the upward fracture growth of 1850 m, the upward mass flux rate toward the overlying Sherwood Sandstone aquifer would increase to $10^7 \text{ kg Cl}^-/\text{yr}$ from below $0.1 \text{ kg Cl}^-/\text{yr}$, creating contaminant plumes within the St. Bees Sandstone and the aquifer layer in 300 year (supporting information Figure 10Sc and Figure 11c).

3.6. Implications and Further Work

This numerical assessment suggests that the hydraulic properties of the geological layers between the Bowland Shale and its overlying aquifers, as well as the upward fracture height growths and fracture aperture, have significant impact on the upward mass flux. Further research should include the field data collection of hydraulic parameters (i.e., hydraulic conductivity, head gradient) of the stratigraphic units overlying the Bowland Shale. This could increase the confidence of model predictions, as the hydraulic parameter values adopted in this study are mainly from shallow pump tests collected for other purposes, which might not be able to adequately represent hydraulic properties of the deep geological layers. In addition, although a

horizontal head gradient was assumed for the entire domain, there is, however, very limited information with regard to the subsurface water flow in the deep geological setting below 1000 m of the ground surface level. With the uncertainty in selected hydraulic conductivities for the multilayered system, this could introduce a bigger uncertainty in the model prediction.

As an initial step for the risk assessment of the complex geological setting of the Bowland Shale, this study did not explicitly include heat and variable-density flow phenomena. The upward brine flux induced by heat, overpressure of shale, and density gradient was, instead, represented by a flux boundary condition, by assuming 250% upward head gradient at the bottom of the domain. Adoption of a modeling approach that explicitly represents the effect of overpressure, heat, and variable-density on fluid flow and chloride movement could increase the accuracy of the model prediction once these data are available. Finally, the collection of new data with regard to the upward fracture height growths and fracture aperture could also increase confidence of the model predictions.

We recognized that water saturation in the shale formation maybe extremely low in some cases due to the occupation of natural gas in the pore space. Hydraulic fracturing could induce variable saturated multiphase fluid and gas flow, as well as mass movement in the fractured shale. To represent this complex flow and solute transport phenomena, sophisticated modeling approaches are required with high computation efforts and extensive field observation data. Due to the lack of the modeling capability and the relevant data, these complex flow and mass transport processes were not accounted for in this study. However, the impact of the gas and variable saturated fluid flow on mass movement toward the overlying aquifers is a future research subject for the risk assessment of hydraulic fracturing. We must stress that potential sources of contaminants risk to the overlying aquifers via the induced fractures may not necessarily come from the hydraulically fractured shale only. It can be from other geological layers near the shale formations which are saturated with saline water.

4. Summary

This numerical assessment suggests that, with a fracture aperture $\leq 200 \mu\text{m}$, the hydraulically fractured Bowland Shale is unlikely to pose risks to its overlying groundwater quality in the Sherwood Sandstone aquifer. With the fracture aperture $\geq 1000 \mu\text{m}$, the upward chloride flux becomes very sensitive to the upward fracture height growth $\geq 1000 \text{ m}$ and the permeability of the multilayer bedrock system. In the event of the upward fracture growth intercepted by the existing faults which create upward fracture-fault conduits connecting the Bowland Shale to the overlying Sherwood Sandstone aquifer directly, the numerical simulations suggest that chloride upward mass flux rates toward the overlying Sherwood Sandstone aquifer could increase to $10^6 \text{ kg Cl}^-/\text{yr}$ in the typical K case and to $10^7 \text{ kg Cl}^-/\text{yr}$ in the low K case, when a constant chloride concentration of $350 \text{ g Cl}^-/\text{L}$ is applied for the brine in the fractured shale. These could potentially pose significant risks to the overlying Sherwood Sandstone aquifer within 100 years for the typical case and within 300 years for the low K case. However, this scenario for upward fracture growth by hydraulic fracturing is extremely unlikely according to the previous studies.

The model study also reveals that the hydraulic properties of the geological layers between the Bowland Shale and the overlying Sherwood Sandstone aquifer have a significant role with regard to the upward mass flux. High permeability layers located between the two geological units can act as barriers to reduce contaminant risk to the overlying groundwater quality. It is evident that the upward mass flux is significantly intercepted by the horizontal mass flux within a 150 m thick high permeable layer of the Collyhurst Sandstone, which is located between the Bowland Shale and its overlying aquifers. The interception by the horizontal mass flux creates a steep salinity gradient within the Collyhurst Sandstone, preventing further upward flux toward the overlying aquifers. This results in a significant reduction of the upward mass flux toward the Sherwood Sandstone aquifer. Sensitivity analyses indicate that impacts of the upward fracture height and the fracture aperture on the upward mass flux become significant in a lower permeability scenario for the multilayered bedrock system.

The fluid injection modeling suggests that bulk hydraulic conductivity of the Bowland Shale before hydraulic fracturing is below $6 \times 10^{-9} \text{ m/s}$, which is of the same order of magnitude as the reported permeability of Marcellus and Barnett shale formation in the United States. Bulk hydraulic conductivity of the Bowland Shale after hydraulic fracturing is in the range of $6 \times 10^{-7} \text{ m/s}$, which is consistent with a report that

hydraulic fracturing increased 100–1000 times of the permeability of the shale formation. The pressure head release profile and mass flux breakthrough curves confirm that the fluid injection during hydraulic fracturing is unlikely to have long-term effects on the flow field in the multilayered bedrock system, as a new steady state flow conditions are expected within ~ 200 h after the cease of the injection. This suggests that impact of fluid and solute transport during the transient stage is short-lived and the steady state flow and solute transport can be used for long-term risk assessment of the hydraulically fractured Bowland Shale.

This study suggests that the upward fracture growths induced by hydraulic fracturing could significantly increase the upward fluid flux rates, particularly those toward the upper layers of the Sandstone aquifers. A rigorous assessment of impact of hydraulically fractured shale formations should not be carried out by the investigation of subsurface water flow only. Instead, a subsurface flow and solute transport approach, which can address the complex flow and solute transport in fractures and rock matrix of the multilayered system, should be adopted for this purpose. Our simulations demonstrate that, although the upward fracture growth substantially increased upward water flux rates by up to 300 times toward the sandstone aquifers, upward mass flux toward the Sherwood Sandstone aquifer have not increased accordingly to pose a risk to water quality in the overlying aquifers.

Acknowledgments

This research is supported by a research grant aided by the Irish Department of Communications, Energy, and Natural Resources under the National Geoscience Programme 2007–2013. The views expressed in this paper are the authors' own and do not necessarily reflect the views and opinions of the Minister of Communications, Energy, and Natural Resources. This paper benefits from numerous discussions with our colleague J.C. Comte. The authors also gratefully thank to Robert McLaren from University of Waterloo (now with Aquanty) for his provision of HydroGeoSphere to this study. We are grateful to Associate Editor D. O'Carroll, T. Gleeson, and two anonymous reviewers of their thorough and constructive comments which significantly improved the work.

References

- Allen, D. J., L. J. Brewerton, L. M. Coleby, B. R. Gibbs, M. A. Lewis, A. M. MacDonald, S. J. Wagstaff, and A. T. Williams (1997), The physical properties of major aquifers in England and Wales, *Br. Geol. Surv. Tech. Rep. WD/97/34*, Environ. Agency R&D Publ. 8, Keyworth, Nottingham.
- Andrews, I. J. (2013), The Carboniferous Bowland Shale gas study: Geology and resource estimation, report, Br. Geol. Surv. for Dep. of Energy and Clim. Change, London.
- Arthur, J., B. Bohm, and M. Layne (2008), Hydraulic fracturing considerations for natural gas wells of the Marcellus Shale, paper presented at The Ground Water Protection Council Annual Meeting, Cincinnati, Ohio.
- Bath, A., H. Richards, R. Metcalfe, R. McCarthney, P. Degnan, and A. Littleboy (2006), Geochemical indicators of deep groundwater movements at Sellafield, UK, *J. Geochem. Explor.*, 90, 24–44.
- Bear, J. (1972), *Dynamics of the Fluid in Porous Media*, Elsevier, N. Y.
- Bense, V. F., T. Gleeson, S. E. Loveless, O. Bour, and J. Scibek (2013), Fault zone hydrogeology, *Earth Sci. Rev.*, 127, 171–192.
- Boyer, E. W., B. R. Swistock, J. Clark, M. Madden, and D. E. Rizzo (2011), The impact of Marcellus gas drilling on rural drinking water supplies, report, The Cent. for Rural Pa., Harrisburg, Pa. Gen. Assem.
- Broderick, J., K. Anderson, R. Wood, P. Gilbert, and M. Sharmina (2011), Shale gas: An updated assessment of environmental and climate change impacts, report, The Co-oper. and Univ. of Manchester, Manchester.
- Cai, Z., D. N. Lerner, R. G. McLaren, and R. D. Wilson (2007), Conceptual analysis of zero-valent iron fracture reactive barriers for remediating a trichloroethylene plume in a chalk aquifer, *Water Resour. Res.*, 43, W03436, doi:10.1029/2006WR004946.
- Cohen, H. A., T. Parratt, and C. B. Andrews (2013), Potential contaminant pathways from hydraulically fractured shale to aquifers, *Ground Water*, 51(3), 317–319.
- Cripps, J. C., and R. K. Taylor (1981), The engineering properties of mudrocks, *Q. J. Eng. Geol.*, 14(4), 325–346.
- Dames and Moore (1999), Numerical groundwater flow and contaminant transport modelling of PCE in the chalk aquifer at Sawston, Cambridgeshire, *Rep. R0125/22427-011-401/SNN/AJW/gw*, Manchester.
- Daneshy, A. (2010), Hydraulic fracture to improve production, *TheWayAhead*, 16(3), 14–17.
- Davies, R. J., S. A. Mathias, J. Moss, S. Hustoft, and L. Newport (2012), Hydraulic fractures: How far can they go?, *Mar. Pet. Geol.*, 37(1), 1–6.
- de Pater, C. J., and S. Baisch (2011), Geomechanical study of Bowland Shale seismicity: Synthesis report, report, Cuadrilla Resour. Ltd., Lichfield, U.K.
- DiGiulio, D. C., R. T. Wilkin, C. Miller, and G. Oberly (2011), DRAFT: Investigation of ground water contamination near Pavillion, Wyoming, report no. EPA 600/R-00/000, U.S. Environ. Prot. Agency, Off. of Res. and Dev. Ada, Oklahoma.
- Flewelling, S. A., and M. Sharma (2014), Constraints on upward migration of hydraulic fracturing fluid and brine, *Ground Water*, 52(1), 9–19.
- Flewelling, S. A., M. P. Tymchak, and N. Warpinski (2013), Hydraulic fracture height limits and fault interactions in tight oil and gas formations, *Geophys. Res. Lett.*, 40, 3602–3606, doi:10.1002/grl.50707.
- Fisher, K., and N. Warpinski (2012), Hydraulic-fracture-height growth: Real data, *SPE Prod. Oper.*, 27(1), 8–19.
- Gassiat, C., T. Cleeson, R. Lefebvre, and J. McKenzie (2013), Hydraulic fracturing in faulted sedimentary basin: Numerical simulation of potential continuation of shallow aquifers over long time scales, *Water Resour. Res.*, 49, 8310–8327, doi:10.1002/2013WR014287.
- Gelhar, L. W., C. Welty, and K. R. Rehfeldt (1992), A critical-review of data on field-scale dispersion in aquifers, *Water Resour. Res.*, 28(7), 1955–1974.
- Harvey, T., and J. Gray (2010), The unconventional hydrocarbon resources of Britain's onshore basins – shale gas, report, Dep. of Energy and Clim. Change, London.
- Hobbs, P. R. N., J. R. Hallam, A. Forster, D. C. Entwisle, L. D. Jone, A. C. Cripps, K. J. Northmore, S. J. Self, and J. L. Meakin (2002), Engineering geology of British rocks and soils-Mudstones of the Mercia Mudstone Group, *Br. Geol. Surv. Res. Rep. RR/01/02*, 106 pp., Keyworth, Nottingham.
- Holliday, D. W. (1986), Devonian and carboniferous basins, in *Geothermal Energy—The Potential in the United Kingdom*, edited by R. A. Downing and D. A. Gray, pp. 84–110, Her Majesty's Stn. Off., London.
- Jones, H. K., et al. (2000), The physical properties of minor aquifers in England and Wales, *Br. Geol. Surv. Tech. Rep. WD/00/4*, 234 pp., Environ. Agency R&D Publ. 68, Keyworth, Nottingham.
- King, G. (2012), Hydraulic fracturing 101: What every representative, environmentalist, regulator, reporter, investor, university teacher, neighbor and engineer should know about estimating frac risk and improving frac performance in unconventional gas and oil wells, paper presented at the SPE Hydraulic Fract. Technol. Conf., Soc. of Pet. Eng., The Woodlans, Tex., 6–8 February.

- Lee, D. S., J. D. Herman, D. Elsworth, H. T. Kim, and H. S. Lee (2011), A critical evaluation of unconventional gas recovery from the Marcellus Shale, northeastern United States, *KSCE J. Civil Eng.*, *15*(4), 679–687.
- Littleboy, A. K. (1995), An approach to the hydrogeological characterization of hard fractured rock, European Commission nuclear science and technology, *Topic Rep./EUR 15959*, European Commission, Luxembourg.
- Loseth, H., L. Wensaas, B. Arntsen, N. M. Hanken, C. Basire, and K. Graue (2011), 1000 m long gas blow-out pipes, *Mar. Pet. Geol.*, *28*(5), 1047–1060.
- McKeown, C., R. S. Haszeldine, and G. D. Couples (1999), Mathematical modelling of groundwater flow at Sellafield, UK, *Eng. Geol.*, *52*(3–4), 231–250.
- Millington, R. J. (1959), Gas diffusion in porous media, *Science*, *130*(3367), 100–102.
- Montgomery, S., D. Jarvie, K. Bowker, and R. Pollastro (2005), Mississippian Barnett Shale, Fort Worth basin, north-central Texas: Gas-shale play with multi-trillion cubic foot potential, *AAPG Bull.*, *89*(2), 155–175.
- Myers, T. (2012), Potential contaminant pathways from hydraulically fractured shale to aquifers, *Ground Water*, *50*(6), 872–882.
- Osborn, S. G., A. Vengosh, N. R. Warner, and R. B. Jackson (2011), Methane contamination of drinking water accompanying gas-well drilling and hydraulic fracturing, *Proc. Natl. Acad. Sci. U. S. A.*, *108*(20), 8172–8176.
- Rutqvist, J., A. P. Rinaldi, F. Cappa, and G. J. Moridis (2013), Modeling of fault reactivation and induced seismicity during hydraulic fracturing of shale-gas reservoirs, *J. Pet. Sci. Eng.*, *107*, 31–44, doi:10.1016/j.petrol.2013.04.023.
- Saiers, J. E., and E. Barth (2012), "Potential contaminant pathways from hydraulically fractured shale aquifers," by T. Myers, *Ground Water*, *50*(6), 826–828.
- Schulze-Makuch, D., D. A. Carlson, D. S. Cherkauer, and P. Malik (1999), Scale dependency of hydraulic conductivity in heterogeneous media, *Ground Water*, *37*(6), 904–919.
- Schurch, M., and D. Buckley (2002), Integrating geophysical and hydrochemical borehole-log measurements to characterize the Chalk aquifer, Berkshire, United Kingdom, *Hydrogeol. J.*, *10*(6), 610–627.
- Schurch, M., W. M. Edmunds, and D. Buckley (2004), Three-dimensional flow and trace metal mobility in shallow Chalk groundwater, Dorset, United Kingdom, *J. Hydrol.*, *292*(1–4), 229–248.
- Shapiro, S. A., O. S. Kruger, C. Dinske, and C. Langenbruch (2011), Magnitudes of induced earthquakes and geometric scales of fluid-stimulated rock volumes, *Geophysics*, *76*(6), WC55–WC63.
- Soeder, D. (1988), Porosity and permeability of easter devonian gas shale, *SPE Form Eval.*, *3*(1), 116–124.
- Tellam, J. H., and J. W. Lloyd (1981), A review of the hydrogeology of British onshore non-carbonate mudrocks, *Q. J. Eng. Geol.*, *14*(4), 347–355.
- The Royal Society and The Royal Academy of Engineering (2012), Shale gas extraction in the UK: A review of hydraulic fracturing, report no. DES2597, London.
- Therrien, R., and E. A. Sudicky (1996), Three-dimensional analysis of variably-saturated flow and solute transport in discretely-fractured porous media, *J. Contam. Hydrol.*, *23*(1–2), 1–44.
- Therrien, R., R. G. McLaren, E. A. Sudicky, and S. M. Panday (2004), *HydroSphere: A Three-dimensional Numerical Model Describing Fully-integrated Subsurface and Surface Flow and Solute Transport*, University of Waterloo.
- U.S. Energy Information Administration (2013a), Annual energy outlook 2013, early release, report, U.S. Dep. of Energy, Washington, D. C.
- U.S. Energy Information Administration (2013b), Technically recoverable shale oil and shale gas resources: An assessment of 137 shale formations in 41 countries outside the United States, report, Dep. of Energy, Washington, D. C.
- U.S. Environmental Protection Agency (1987), Report to congress: Management of wastes from the exploration, development, and production of crude oil, natural gas, and geothermal energy, report no. EPA/530-SW-88-003, U.S. Environ. Protect. Agency, Washington, D. C.
- Vidic, R. D., S. L. Brantley, J. M. Vandenbossche, D. Yoxtheimer, and J. D. Abad (2013), Impact of Shale gas development on regional water quality, *Science*, *340*, doi:10.1126/science.1235009.
- Warner, N. R., R. B. Jackson, T. H. Darrah, S. G. Osborn, A. Down, K. Zhao, A. White, and A. Vengosh (2012), Geochemical evidence for possible natural migration of Marcellus Formation brine to shallow aquifers in Pennsylvania, *Proc. Natl. Acad. Sci. U. S. A.*, *109*(30), 11,961–11,966, doi:10.1073/pnas.1121181109.
- Williams, J. H. (2010), Evaluation of well logs for determining the presence of freshwater, saltwater, and gas above the Marcellus Shale in Chemung, Tioga, and Broome Counties, *Rep. 2010–5224*, U.S. Geol. Surv. Sci. Invest., N. Y.
- Zoback, M., S. Kitasei, and B. Copithorne (2010), Addressing the environmental risks from shale gas development, report, Worldwatch Inst., Washington, D. C.